Novel Pyrazolo[3,4-*c*]pyridine Antagonists with Nanomolar affinity for A$_1$ / A$_3$ Adenosine Receptors: Binding Kinetics and Exploration of their Binding Profile Using Mutagenesis Experiments, MD simulations and TI/MD calculations

Margarita Stampelou, [†,x] Anna Suchankova, [‡,x] Eva Tzortzini, [†] Lakshiv Dhingra, [‡] Kerry Barkan,[‡] Nikolaos Lougiakis, [†] Panagiotis Marakos, [†] Nikole Pouli,[†*] Graham Ladds, [‡,y,*] Antonios Kolocouris [†,y,*]

[†] Laboratory of Medicinal Chemistry, Section of Pharmaceutical Chemistry, Department of Pharmacy, School of Health Sciences, National and Kapodistrian University of Athens, Panepistimiopolis-Zografou, 15771 Athens, Greece
[‡] Department of Pharmacology, University of Cambridge, Tennis Court Road, Cambridge, CB2 1PD, UK.

[x] These authors contribute equally
[y] These authors contribute equally

Abstract

Drugs targeting the four adenosine receptor (AR) subtypes can provide "soft" treatment of various significant diseases. Even for the two experimentally resolved AR subtypes the description of the orthosteric binding area and structure-activity relationships of ligands remains a demanding task due to the high similar amino acids sequence but also the broadness and flexibility of the ARs binding area. The identification of new pharmacophoric moieties and nanomolar leads and the exploration of their binding area with mutagenesis and state-of-the-art computational methods useful also for drug design purposes remains a challenging aim for all ARs.

Here, we identified several low nanomolar ligands and potent competitive antagonists against A_1R / A_3R, containing the novel pyrazolo[3,4-c]pyridine pharmacophore for ARs, from a screen of an *in-house* library of only 52 compounds, originally designed for anti-proliferative activity. We identified **L2-L10, A15, A17** with 3-aryl, 7-anilino and a electronegative group at 5-position as low micromolar to low nanomolar A_1R / A_3R antagonists. **A17** has for A_1R K_d = 5.62 nM and a residence time (RT) 41.33 min and for A_3R K_d = 13.5 nM, RT = 47.23 min. The kinetic data showed that compared to the not potent or mediocre congeners the active compounds have similar association, for example at A_1R K_{on} = 13.97 x10^6 M^{-1} (**A17**) vs K_{on} = 3.36 x10^6 M^{-1} (**A26**) but much lower dissociation rate K_{off} = 0.024 min^{-1} (**A17**) vs 0.134 min^{-1} (**A26**). Using molecular dynamics (MD) simulations and mutagenesis experiments we investigated the binding site of **A17** showing that it can interact with an array of residues in transmembrane helix 5 (TM5), TM6, TM7 of A_1R or A_3R including residues $E^{5.30}$, $E^{5.28}$, $T^{7.35}$ in A_1R instead of $Q^{5.28}$, $V^{5.30}$, $L^{7.35}$ in A_3R. A striking observation for drug design purposes is that for L250$^{6.51}$A the binding affinity of **A17** significantly increased at A_1R.

A17 provides a lead representative of a promising series and by means of the Thermodynamics Integration coupled with MD simulations (TI/MD) method, first applied here on whole GPCR-membrane system and showing a very good agreement between calculated and experimental relative binding free energies for A_1R and A_3R (spearman rank correlation p = 0.82 and 0.84, respectively), and kinetic experiments can lead to ligands with improved profile against ARs.

Introduction

Adenosine a naturally occurring purine nucleoside, is the endogenous agonist of adenosine receptors (ARs) which mediate the actions of adenosine. [1] They are G protein-coupled receptors (GPCRs) comprising four subtypes; A_1, A_{2A}, A_{2B} and A_3. $A_{2A}R$ and $A_{2B}R$ subtypes act synergistically with the G_s proteins resulting in the stimulation of the adenylyl cyclase, and therefore, the increase of 3',5'-cyclic adenosine monophosphate (cAMP) levels. In contrast, A_1R and A_3R subtypes inhibit the adenylyl cyclase and decrease cAMP levels within cell by coupling to G_i or G_q family of G proteins. $A_{2A}R$ has been extensively studied over the last few decades as it had been the only one of four subtypes that had been solved from 2008 [2–9] until 2017 when the X-ray structure of A_1R was also solved. [10,11]

The binding mode of agonists, like adenosine and 5'-N-ethylcarboxamidoadenosine (NECA), [2–4] as well as of several antagonists [5–9] has been revealed in crystallographic A_{2A} structures since 2008 or the complexes with G_s protein solved using electron cryo-microscopy in 2018. [4] These experimental structures can help to understand the binding interactions of ARs with ligands and provide templates for structure-based drug design as other groups [12–18] and our [19] group performed. For example, in our previous work, from *in silico* screening of Maybridge HitFinder Library [19] using the experimental structure of $A_{2A}R$ with ZM241385 (PDB ID 3EML) [5] we identified new hits, with low micromolar affinities against A_3R measured using radio-labeled assays. [19] The affinities were in most cases consistent with antagonistic receptor activities determined using inhibition of cAMP accumulation. [20] With the agonist NECA and the specific N6-(3-iodobenzyl)-adenosine-5'-N-methylcarboxamide (IB-MECA) for A_3R and our identified antagonists we investigated structural features of the experimentally unresolved A_3R orthosteric binding area using MD simulations with an homology model for A_3R, mutagenesis and functional assays. [20–22]

Different therapeutic applications have been identified in preclinical and clinical studies of A_1R antagonists as potassium-sparing diuretic agents with kidney-protecting properties. [23,24] This type of compounds can be useful in the treatment of chronic heart diseases. [25] A_1R antagonists may offer a therapeutic opportunity for chronic lung diseases such as asthma, chronic obstructive pulmonary disease (COPD) and pulmonary fibrosis. [23,26] The observation of the effects of caffeine, a classical non-selective adenosine antagonist, on the central nervous system (CNS), [23] such as improvement of awareness and learning, encouraged the search of selective antagonists endowed with CNS activity. Selective A_1R antagonists induce cognition enhancement, [23] leading to a general improvement in memory performance, and these actions are potentially useful in the treatment of dementia and anxiety disorders. [27] Moreover, it have been reported that treatment with the A_1R antagonist CPT (8-cyclopentyl-1,3-dimethylxanthine) in a model of Parkinson's disease produced a dose dependent improvement in locomotion, suggesting that, although the role of A_1R in Parkinson's disease is still unclear, the A_1R antagonism may produce therapeutic effects, particularly at the beginning of treatment. [28]

The A_3R subtype, coupled to G_q proteins, stimulates phospholipase C activity, thus enhancing intracellular calcium levels. [29] This AR subtype modulates mitogen-activated protein kinase (MAPK) pathways, that can be both activated or inhibited, depending on the cellular model. The A_3R influencing MAPK activity explains the role of this receptor on cell proliferation and differentiation, [29,30] and in tumor development and progression. A_3R is overexpressed in several types of cancer cells, and is thus considered as a possible biological marker for tumors. [29] It is well established that MAPK pathways are involved in tubulointerstitial fibrosis which is a common feature of kidney diseases leading to chronic renal failure. [31] In a recent study, the potent and selective A_3R antagonist LJ-1888 ((2R,3R,4S)-2-[2-chloro-6-(3-iodobenzylamino)-9H-purine-9-yl]tetrahydrothiophene-3,4-diol) blocked the development and attenuated the progression of renal interstitial fibrosis. [31] These findings suggested that A_3R antagonists might become new therapeutic tools for the treatment of both chronic renal disease and acute renal ischemia and reperfusion injury. [32] A_3R antagonists have demonstrated efficacy in eye pathologies. [29] It has been reported that the potent A_3R antagonist MRS1220 (N-[9-chloro-2-(2-furanyl)-1,2,4-triazolo[1,5-c]quinazolin-5-yl]benzeneacetamide) prevents oligodendrocyte damage and myelin loss triggered by ischemia or by activation of the A_3R in the rat optic nerve. [33] Hence, blockage of the A_3R has proven to be useful for the treatment of diverse diseases, however its role is still to be elucidated under other pathophysiological conditions, such as inflammation, cancer or pain. [29] The identification of new potent and selective ligands which clarify the therapeutic potential arising from blocking or stimulating the A_3R remains an attractive objective. [29,34]

There has been emerging the realization that selecting ligands based on their affinity, an equilibrium parameter, does not necessarily predict in vivo efficacy. Kinetic profiling in drug discovery process allows resolving ligand-receptor interactions into both molecular recognition (depending on association constant K_{on}) and complex stability (depending on ligand's dissociation constant K_{off}) provides additional parameters of drug candidates with the residence time (RT= $1/K_{off}$) proposed to be the more relevant selecting criterion. [35,36] In fact, a ligand's kinetic properties may provide a better indication of how a ligand will perform in vivo. Thus, the identification of ligands with desired thermodynamic and kinetic binding characteristics provide lead compounds for further development and chemical probes for the study of these receptors. Selected antagonists for A_1R [35] and A_3R [37,38] are shown in Scheme 1.
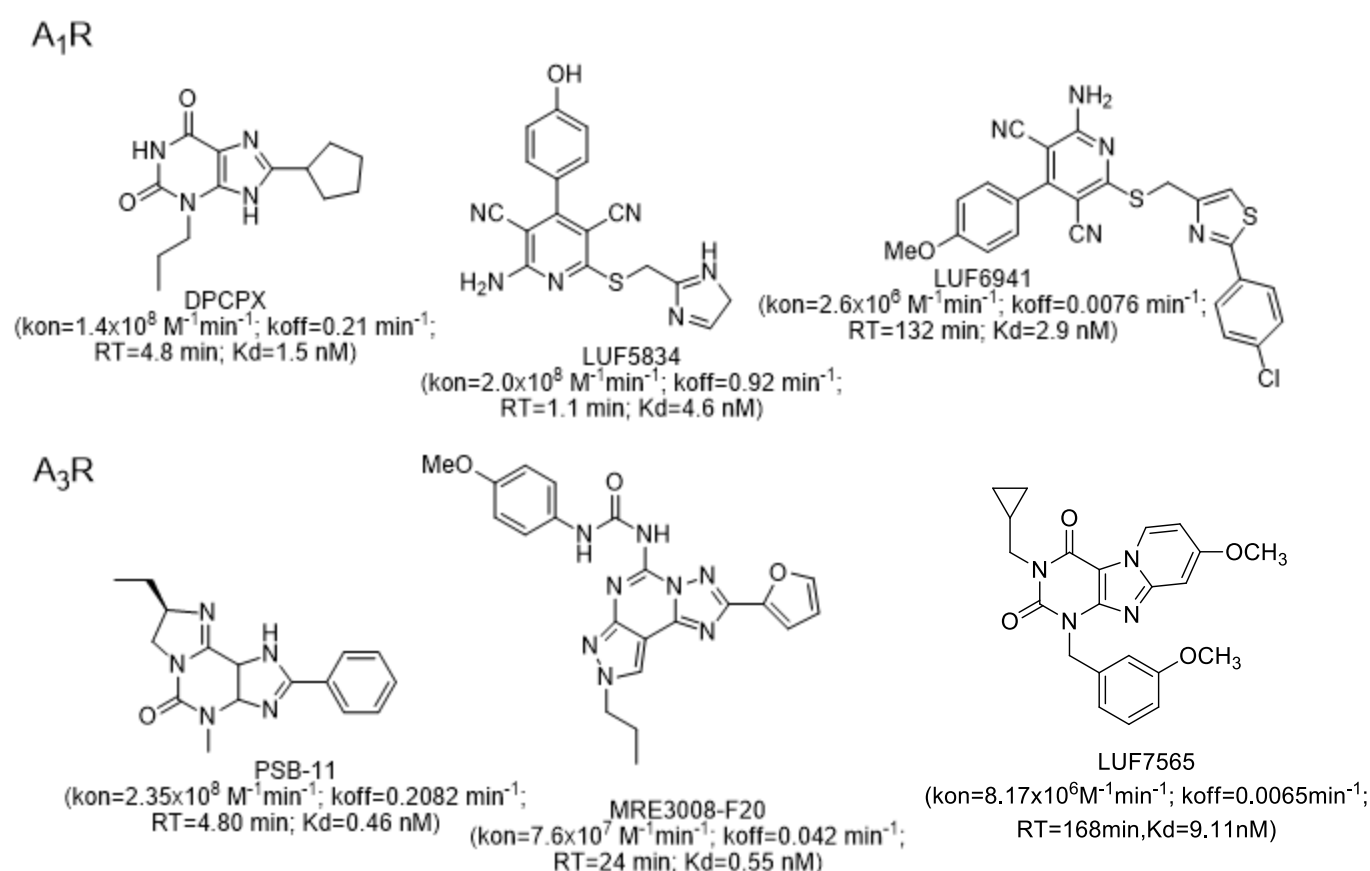
Scheme 1. Association (K_{on}) and dissociation (K_{off}) rate constants of selected A_1R (DPCPX, [39] LUF5834, [40] LUF6941[41]) and A_3R ligands (PSB-11, [42] MRE3008-F20, [43] LUF7565 [38]).

In this work we biologically screened against ARs using functional assays 7 classes of molecules comprising by 52 compounds (Table S1). The tested compounds belong to our *in-house* compounds library and were aromatic nitrogen heterocycles with originally purposed for anti-proliferative activity, [37,46,47] against angiogenesis, [48] as fluorescence tracers in cells, [49] against hepatitis B virus, [50] and nucleosides originally tested against adenosine deaminase, [51] hepatitis C virus, [52] and human cytomegalovirus. [53] We found that pyrazolo[3,4-c]pyridine, is a novel heterocyclic ring that bind ARs having antagonistic activity to A_1R and A_3R with potential for further development. We investigated experimentally for the identified two classes of pyrazolo[3,4-c]pyridines their (a) pharmacological profile using functional assays, (b) binding interactions and binding kinetic profile using, correspondingly, molecular dynamics (MD) simulations and mutagenesis experiments, and competition binding experiments with the NanoBRET [20] (Nano Bioluminescence resonance energy transfer) method. The kinetic study of one class of these compounds showed high K_{on} and low K_{off} providing nanomolar affinities. We identified the low nanomolar ligand and competitive antagonist **A17** against both A_1R and A_3R.

To further characterize the interactions of these ligands with the A_1R and A_3R orthosteric binding area, we performed also binding free energy calculations using the approximate Molecular Mechanics-Generalized Born Surface Area (MM-GBSA) method [54] with an implicit membrane [55] and by taking into account the waters inside the binding area. [56] In order to confirm reliably the suggested binding site of the studied pyrazolo[3,4-c]pyridines we compared the experimentally measured relative binding free energies in the same series, with calculated values using the Thermodynamic Integration coupled with MD simulations (TI/MD) method and a thermodynamic cycle. This is the first time that the TI/MD method including the whole membrane was applied in a ligands-GPCR-bilayer system. The accuracy of relative binding free energies calculation for ligands-GPCR systems have been studied previously using the Free-Energy Perturbation coupled with MD simulations (FEP/MD) method and a thermodynamic cycle. [57]

Biological methods

Cell lines

Stable Flp-In-CHO cell lines expressing the WT A_3R were generated and maintained as previously described. [58,59] CHO-K1 cells stably expressing WT A_1R, $A_{2A}R$ or $A_{2B}R$ were routinely cultured in Hams F-12, supplemented with 10% Foetal bovine serum (FBS). All were annually checked for mycoplasma infection using an EZ-PCR mycoplasma test kit (Biological Industries, Kibbutz Beit-Haemek, Israel). Production and analysis of the mutant versions of the A_1R were as described in ref [60].

Compounds

NECA was purchased from Sigma-Aldrich and dissolved in dimethyl sulfoxide (DMSO). The 52 compounds tested were available from an *in-house* library of the Laboratory of Medicinal Chemistry, Section of Pharmaceutical Chemistry, Department of Pharmacy, National and Kapodistrian University of Athens.

cAMP accumulation assay

cAMP inhibition experiments were performed using a LANCE® cAMP kit as described previously. [58,59] Briefly, Flp-In-CHO cells expressing WT A_3R and CHO-K1 cells expressing WT A_1R, $A_{2A}R$ or $A_{2B}R$ were seeded in a white 384-well optiplate at a density of 2,000 cells per well and stimulated for 30 min with a range of NECA concentrations, with or without potential antagonists, in the presence of 0.1% BSA and 25 µM rolipram, and 10 µM forskolin (to enable detection of A_1R- or A_3R-mediated inhibition of cAMP). For the initial screening IC_{80} (6.32 nM) of NECA was used. Since the $A_{2A}R$ and $A_{2B}R$ promote cAMP accumulation, [61] the addition of forskolin was not included when assaying these receptors.

Schild analysis

NECA concentration-dependent response curves were constructed in the presence or either DMSO alone or 1 µM test compound or 1 µM MRS1220 (9-chloro-2-(2-furanyl)-5-((phenylacetyl)amino)-[1,2,4]triazolo[1,5-c]quinazoline). NECA concentrations ranged from 1 pM to 1 µM. Estimates of the EC_{50} values in the presence and absence of the antagonist were determined using the three-parameter logistic equation built into Prism.

NanoBRET assays for binding

NanoBRET competition binding assays were conducted to determine the affinity (pK_i) of various potential antagonists at the A_1R and A_3R as described previously. [20] For both the A_1R and A_3R, the CellAura fluorescent A_3R antagonist (CA200645) with a xanthine amine congener (XAC) structure was used at 20 nM and 5nM concentration for A_1R and A_3R, respectively, since it has a slow off rate. Kinetic data was fitted with the 'kinetic of competitive binding' model (see ref. [62]; built into Prism) to determine affinity (pK_i) values and the association rate constant (K_{on}) and dissociation rates (K_{off}) for unlabelled A_3R antagonists. In agreement with our previous studies [60,20] we determined the pK_d of CA200645 at the A_1R to be 18.29 ± 2.4 nM and at the A_3R 26.95 ± 3.2 nM. [20] The BRET ratio at 10 min poststimulation was fitted with the "one-site–K_i model" derived from the Cheng and Prusoff correction, built into Prism to determine the affinity (pK_i) constant at equilibrium values for all unlabelled antagonists at the A_1R and A_3Rs.

Data and Statistical analysis

All *in vitro* assay data were analyzed using Prism 9.0 (GraphPad software, San Diego, CA), with all dose-inhibition curves being fitted using a three-parameter logistic equation to calculate response range and pIC_{50}/pEC_{50}. Experimental design ensured random distribution of treatments across 96/384-well plates to avoid systematic bias. Agonist stimulation alone was used as an intrinsic control across all experiments. Dose-inhibition/dose-response curves were normalized to forskolin stimulation ($A_{2A}R$ and $A_{2B}R$) or forskolin inhibition (A_1R and A_3R) relative to NECA (agonist allowing comparison across AR subtypes), expressed as percentage forskolin inhibition for G_i-coupled A_1R and A_3R (1 µM or 10 µM, respectively) or stimulation for $A_{2A}R$ and $A_{2B}R$ (100 µM, representing the maximum cAMP accumulation of the system), relative to NECA. For cAMP

experiments on A_1R mutants, data was normalized to 100 µM forskolin, representing the maximum cAMP accumulation possible for each cell line.

Schild analysis was performed to obtain, the dissociation constant (pK_d,) using eq. (1) [63]

$$\frac{D'}{D} = 1 + [A]K_2, \tag{1}$$

where D' and D = IC_{50} values of NECA with and without antagonist present, respectively, [A] = the concentration of antagonist present, and K_2 = the affinity constant (K_A) of the antagonist used. [63] Receptor binding kinetics was determined as described previously [20] using the Motulsky and Mahan method [62] (built into Prism 9.0) to determine the test compound association rate constant and dissociation rate constant. The K_{on} and K_{off} values for binding of CA200645 at the A_1R were determined to be (A_1R) K_{on} = 3.67 ± 0.34 x 10^6 $M^{-1}min^{-1}$ and K_{off} = 0.06715 ± 0.0045 min^{-1} and (A_3R) K_{on} = 2.86 ± 0.45 x 10^6 $M^{-1}min^{-1}$ and K_{off} = 0.064 ± 0.0023 min^{-1}. These values are in agreement with previous estimates at both receptors. [64] The data and statistical analysis comply with the recommendations on experimental design and analysis in pharmacology. [65] Statistical significance (*, $p < 0.05$;**, $p < 0.01$;***, $p < 0.001$, ;****, $p < 0.0001$) was calculated using a one-way ANOVA with a Dunnett's post-test for multiple comparisons. Compounds taken forwards for further experiments after initial screening were identified as having the highest statistical significance (p value of 0.001 (***) or <0.0001 (****)). All statistical analysis was performed using Prism 9.0 on data which were acquired from experiments performed a minimum of five times, conducted in duplicate.

Computational Biochemistry

3D Similarity Calculations

All of the 3D similarity calculations were performed with Canvas program (Schrödinger Release 2021-1: Canvas, Schrödinger, LLC, New York, NY, 2021). [66] The similar compounds structure was ranked according to the TanimotoCombo [67] coefficient as metric.

Molecular Docking Calculations

The molecular docking calculations of the fourteen tested pyrazolo[3,4-c]pyridines **A15, L2-L10, A17, L12, L15, L21, A26** with structures shown in Table 1 (for the protocol used for the preparation of models of the tested ligands see the Supporting Information) with A_1R and A_3R were performed using GOLD software [68] (GOLD Suite, Version 5.2; Cambridge Crystallographic Data Centre: Cambridge, U.K., 2015. GOLD Suite, version 5.2; Cambridge Crystallogr. Data Cent. Cambridge, U.K., 2015) and ChemScore [69] as the scoring function. The models of A_1R and A_3R WT A_1R - PSB36 [10] and WT A_3R - ZM241385 (see Supporting Information for the description of the generation of these protein complexes) were used as templates for the molecular docking calculations of the antagonists to the binding area of each of the receptors. Each compound was docked in the binding site of ZM241385 in the A_3R-ZM241385 model or DU172 in A_1R-DU172 model in an area of 15 Å around the ligand using the experimental coordinates of ZM241385 or DU172 and 20 genetic algorithm runs were applied for each docking calculation. The top-scoring docking poses were used for MD simulations to investigate the binding profile of the tested pyrazolo[3,4-c]pyridines at A_1R and A_3R.

MD Simulations

Each protein-ligand complex was inserted in a pre-equilibrated hydrated 1-palmitoyl-2-oleoyl-*sn*-glycero-3-phosphoethanolamine (POPE) membrane bilayer according to OPM (Orientations of Proteins in Membranes) database. [70] The orthorhombic periodic box boundaries were set 12 Å away from the protein using the System Builder utility of Desmond v4.9 (Schrödinger Release 2021-1: Desmond Molecular Dynamics System, D. E. Shaw Research, New York, NY, 2021. Maestro-Desmond Interoperability Tools, Schrödinger, New York, NY, 2021). The membrane bilayer consisted by ca. 170 lipids and 16,000 TIP3P [71] water molecules. Sodium and chloride ions were added randomly in the water phase to neutralize the system and reach the experimental salt concentration of 0.150 M NaCl. The total number of atoms of the complex was approximately 75,000 and the simulation box dimensions was (88 x 76 x 113Å^3). We used the Desmond Viparr tool to assign the amber99sb [72,73] force field parameters for the calculation of the protein, lipids and intermolecular interactions, and the Generalized Amber Force Field (GAFF) [74] parameters for the ligands. Ligand atomic charges were computed using the RESP [75] fitting for the electrostatic

potentials calculated with Gaussian03 [76] at the HF/6-31G* [77] level of theory and the antechamber of AmberTools18. [78]

100 ns MD simulations at constant pressure (NPT) were performed for the 14 most interesting ligands **A15, L2-L10, A17, L12, L15, L21, A26** (Table 1) in complex with A_1R or A_3R embedded in POPE bilayers using Desmond v4.9 software, the Desmond MD algorithm [79] with amber99sb [75] force field to investigate their binding interactions. The protocol used to calculate interactions and run the MD simulations and the visualization of the trajectories is described in the Supporting Information. Within the 100ns-MD simulation time, the total energy and RMSD of the protein backbone C_α atoms reached a plateau, and the systems were considered equilibrated and suitable for statistical analysis (Figure S3). The $RMSD_{prot}$ values were between 2-3 Å except in cases of the ligands **L8, L9** which having an increased girth produced $RMSD_{prot}$ values 3-3.5 Å.

Three MD simulation repeats were performed for each complex using the same starting structure and applying randomized velocities. All the MD simulations with Desmond software were run on GTX 1060 GPUs in lab workstations or the ARIS Supercomputer.

MM-GBSA calculations

As is described in the Supporting Information, the MD simulation trajectories were used for the calculation of approximate binding free energies of ligand – protein complexes using the 1-trajectory MM-GBSA [54,92] method, the OPLS2005 [82,83] force field and 20 waters in the vicinity of the ligand . The MD trajectories were processed with the Python library MDAnalysis [84] in order to extract the 20 water molecules closest to any atom in the ligand [85] for each of the 501 frames. We applied a dielectric constant $\varepsilon_{solute} = 1$ to the binding area and to account for the lipophilic environment of the protein an heterogeneous dielectric implicit membrane model was used along the bilayer z-axis. [98]

Alchemical TI/MD binding free energies calculated with the MBAR method

The principle of the TI [87] method has been well described in many references while the calculation of relative protein-ligand binding free energy using alchemical transformations relies on a thermodynamic cycle, [88–90] ie. using the free energy ΔA values obtained for the transformations of the ligands in the bound (b) and the solvent (s) (water) state, $\Delta A_{0,1}(b)$ and $\Delta A_{0,1}(s)$, respectively, according to eq. (2)

$$\Delta\Delta A_{0\rightarrow 1} = \Delta A_{0\rightarrow 1}(b) - \Delta A_{0\rightarrow 1}(s) \qquad (2)$$

For the TI/MD calculations, the relaxed complexes of compounds **A15, L3-L6, L8, L9, A17, L12, A26** at A_1R and A_3R from the 100ns-MD simulations in a POPE lipid bilayer with the amber99sb [75] force field were used as starting structures for the calculations of the alchemical transformations described in Table 3. TI/MD calculations were also performed for the ligands in solution.

Setups were performed with CHARMM-GUI [91] using structures of the complexes that were already equilibrated from the 100ns-MD simulations with Desmond and amber ff99sb [75] force field. The relaxed complexes were embedded in a POPE lipid bilayer extending 12 Å beyond the solutes using the CHARM-GUI web-based graphical user tool. [91] Sodium and chloride ions were randomly added in the aqueous phase to neutralize the system based on a Monte-Carlo approach, as implemented in CHARMM-GUI. [91] Each ligand-A_1R or -A_3R complex in the bilayer was processed by the LEaP module in AmberTools18 under the Amber18 software package. [92] Proteins, ligands, and water were described with ff14sb [93] GAFF1.8, [74] and TIP3P force fields, [71] respectively, and intermolecular interactions with ff14sb [93] force field. Atom types, bonded and van der Waals parameters for ligands were added using Antechamber [94] and Parmchk2 in the Amber18 tool set. [92] Partial charges for ligands were obtained using RESP [75] fitting for the electrostatic potentials calculated with Gaussian03 [76] at the Hartree-Fock (HF)/6-31G* [77] level of theory and the antechamber of AmberTools18. [92]

For each calculation, the 1-step protocol was performed, ie. disappearing one ligand and appearing the other ligand simultaneously, and the electrostatic and van der Waals interactions are scaled simultaneously using softcore potentials from real atoms that are transformed into dummy atoms. [90] Alternatively, in the 3-step "decharge-vdW-recharge" protocol, the atoms of the first ligand are first decharged, then undergo a van der Waals interactions transformation using softcore potentials, and then recharged to the final state (second ligand). [90] The 1-step protocol is a less computational expensive and more accurate approach to free energy estimates

according to recent studies. [106] However, for the **L9 → L8** transformation the 3-step protocol was applied because it has been observed that TI calculation converges poorly with 1-step protocol if the substituent that is involved in the transformation include a large numbers of atoms. [107]

For each λ a 500 ps constant volume equilibration (NVT) was followed by 2 ns NVT production simulation without restraints. Production simulations recalculated the potential energy at each λ value every 1 ps for later analysis with MBAR. [102,103] (See Supporting Information for details of the TI/MD simulations protocol). Two repeats were performed for the TI/MD calculation for each alchemical transformation shown in Table 3. Reference MD simulations were run corresponding to the initial and final states for each system to inspect them.

The alchemical binding free energies for the pairs of ligands bound to A_1R or A_3R (Table 3) were computed using the MBAR method [102] and applying a thermodynamic cycle, ie. using the ΔG values obtained for the transformations of the ligands in the bound (b) ($\Delta G_{0,1}(b)$) and the solvent (s) (water) state, respectively, $\Delta G_{0,1}(b)$ and $\Delta G_{0,1}(s)$, according to eq. (2). Experimental relative binding free energies ($\Delta\Delta G_{b,exp}$) were estimated using the experimental binding affinities pK_d in Table 1 according to eq. (3)

$$\Delta\Delta G_{b,exp\ 0\to1} = -1.9872\ T\ (pK d, 1 - pK d, 2) \qquad (3)$$

Results and Discussion

Compounds Selection

We set out to conduct a functional screen initially of 30 compounds from our *in-house* library for the identification of A_3R ligands (Table S1) since their structure had a similarity, computed based on the TanimotoCombo coefficient (Tc) [67] values, with compounds in CHEMBL [117] database reported mainly as A_3R ligands. Thus, the 7-anilino-3-phenyl pyrazolo-[3,4-*c*]pyridines have Tc = 0.4 compared to 9-anilino-imidazo[4,5-*c*]quinoline A_3R antagonists, [110] the 3-acetamido-5-anilino pyrazolo-[3,4-*c*]pyridines have Tc = 0.2-0.3 compared to 2,4-diaminoquinazoline A_3R antagonists, [111] the N-piperazinyl-acetamides of aminopyridinoquinazolines have Tc = 0.22-0.35 compared to N-piperazinyl-acetamideo-aminopyrimidines with antagonistic activity against all ARs, [112] nucleoside derivatives have Tc = 0.3-0.6 compared to agonists or antagonists of all ARs. [113–116]

Biological Results

Screening the in-house library using functional assays revealed 12 new leads as ARs antagonists

For our screen [58,59] the A_3Rs were expressed in Flp-In™ CHO cells. In order to allow the A_3R mediated $G_{i/o}$ response to be determined, the cells were co-stimulated for 30 minutes with 10 μM forskolin (which promotes cAMP production by activating adenylyl cyclase), [61] the predetermined IC_{80} of NECA (which reduces forskolin-induced cAMP production by agonizing the G_i-coupled A_3R) and either DMSO (negative control) or 1 μM tested compound. A putative antagonist would diminish NECA's ability to inhibit forskolin-induced cAMP production, resulting in an elevated cAMP level when compared to DMSO; this was confirmed by the positive control MRS 1220, a known A_3R antagonist (Table 1). From this functional screen we identified four compounds, **A15**, **A17**, **A26** and **A45** as potential A_3R antagonists. The nucleoside **A45** was discontinued in the study since it showed the weakest activity (*p* = 0.0176 vs NECA alone; Figure S1A, Table S1). Of the three remaining compounds, **A15** and **A17** shared the same scaffold (pyrazolo[3,4-c]pyridine) and similar substitution pattern, ie. they are 3-phenyl-7-anilino(pyrazolo[3,4-c]pyridines), while **A26** has the same scaffold but distinct substitution pattern since it is a 3- acetamido-5-anilino(pyrazolo[3,4-c]pyridine.

The 3 new lead compounds have A_1R and A_3R subtype selectivity

The similarities between the four AR subtypes often results in reduced selectivity of potential antagonists. As we described previously [20] we utilized A_3R Flp-In CHO cells or CHO-K1 cells expressing A_1R, $A_{2A}R$, $A_{2B}R$ incubated with a single high concentration of potential antagonist (10 μM) and increasing concentrations of NECA to explore the subtype selectivity of **A15**, **A17** and **A26** at the different ARs in a functional cAMP assay. Both **A15** and **A26** showed a lack of efficacy at the NECA-stimulated $A_{2A}R$ and $A_{2B}R$ but were able to antagonise the A_1R, although **A17** showed weaker efficacy than **A26** (Figure 1). **A17** also was able to antagonise the A_1R alongside the A_3R with high efficacy (Table 1) but did also display, very weak efficacy at the $A_{2B}R$ (pK_d = 5.49 ±0.17).

These data indicate that all three compounds showed high subtype selectivity for both the A_1R and A_3R (Figure 1).
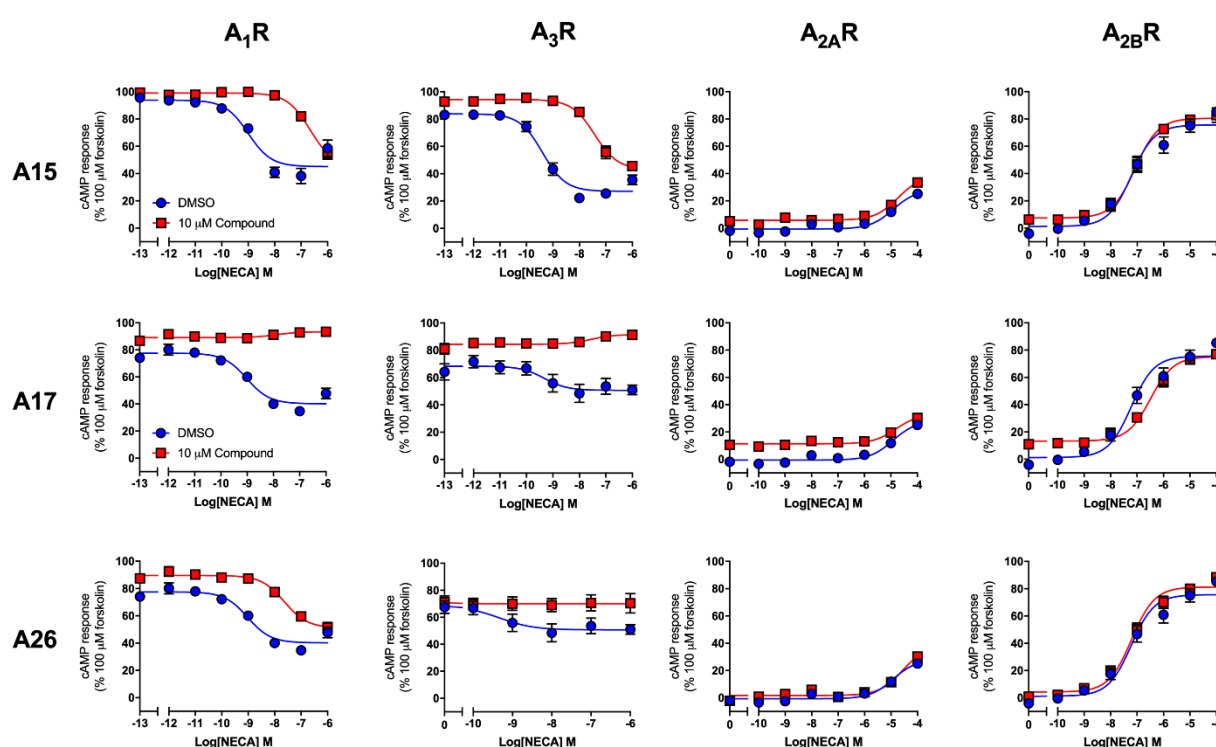

Figure 1. Selectivity of **A15**, **A17** and **A26** at individual AR subtypes (A_1R, $A_{2A}R$, $A_{2B}R$, A_3R). cAMP accumulation or inhibition in response to varying NECA concentration in the absence (blue) or presence of 10 μM tested compound (red) and forskolin for G_i-coupled receptors.

*Additional screen based upon **A15/A17** and **A26** revealed pyrazolo[3,4-c]pyridine as novel scaffold for the development of AR antagonists*

Having identified that **A15/A17** and **A26** have a potential scaffold with which to design A_1R/A_3R antagonists, we performed a second round of compounds screening only using **A15/A17** and **A26** derivatives. Using the same experimental set up as described previously, initially only using A_3R Flp-In CHO cells we screened an additional 22 compounds at 1 μM. Compounds **L1-11** were derivatives of **A15/A17** and **L12-L22** derivatives of **A26** (Table S1) From this screen 10 additional compounds (Table S3) were identified as statistically significant potential antagonists at the A_1R/A_3R through their ability to elevate cAMP accumulation when compared to forskolin and NECA co-stimulation (Figure S1B). All 11 compounds showed a lack of efficacy at the NECA-stimulated $A_{2A}R$ and $A_{2B}R$ except for **L4** which, analogous to **A17**, showed very weak efficacy at the $A_{2R}B$ ($pK_d = 5.77 \pm 0.12$; Figure S2, Tables S2, S4) but were able to antagonise the A_1R or A_3R. The 11 pyrazolo[3,4-c]pyridines, **A15/A17**, **L2-L10** have an alkyl or phenyl group at 3-position, an anilino group at 7-position and a cyano-, or a chloro- or an aminomethyl or N-(arylmethyl)-2-aminomethyl group at 5-position (Table 1). In **A26** and its analogues **L12** and **L15** or **L21** the pyrazolo[3,4-c]pyridine is substituted with 3-(anilinoacetamido) and 3-(N-aminobenzoyl), respectively. In **A26**, **L12**, **L15** or **L21** a 5-anilino group or 7-(N- cyclohexanylamino) is also present.

Functional activities measurement of the 15 pyrazolo[3,4-c]pyridines identified nanomolar antagonists for A_1R, A_3R

Full inhibition curves were obtained for compounds **A15**, **A17**, **L2-L10**, **A26**, **L12**, **L15**, **L21** by stimulating cells with 10 μM forskolin and measuring forskolin-induced cAMP accumulation in CHO-K1-A_1R or A_3R Flp-In CHO cells in the presence of NECA in a range of concentrations (10^{-13} M to 10^{-4} M), and either DMSO or 1 μM potential antagonist (Figure 2). All compounds caused a reduction in NECA potency at the A_3R, characteristic of competitive antagonism all-be-it with varying extents (Table 1). Moreover, some of the compounds also showed antagonism at the the A_1R although compounds **L5**, **A26** displayed only weak effects on NECA potency while **L21** was inactive (Table 1, Table S2, Figure 2).
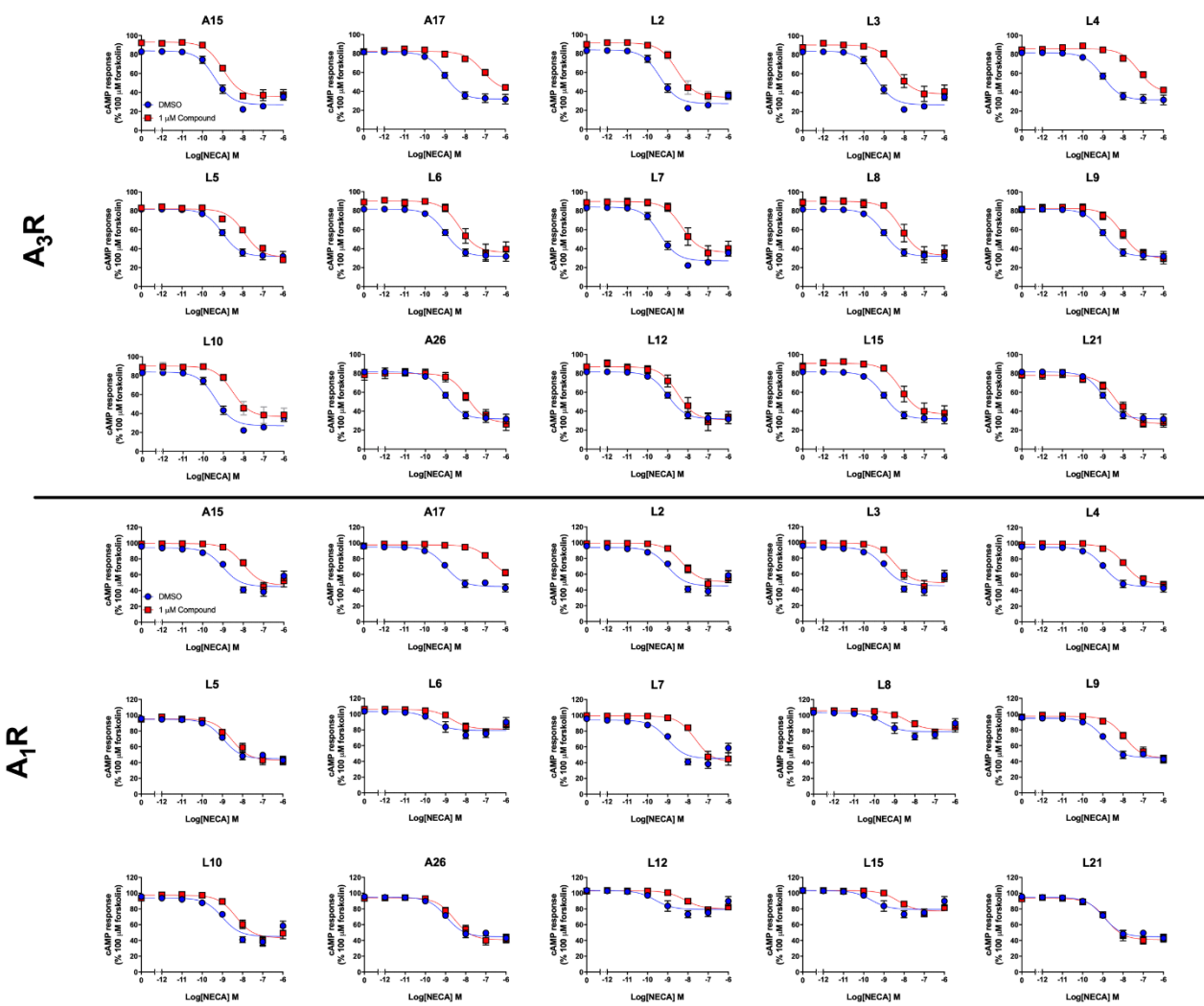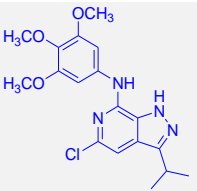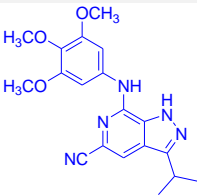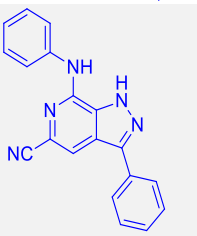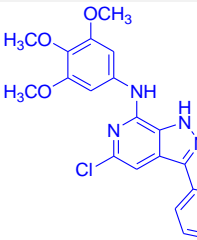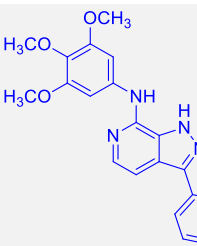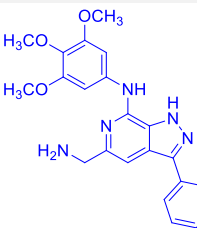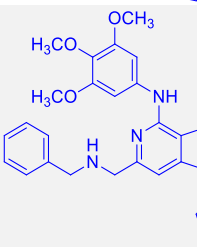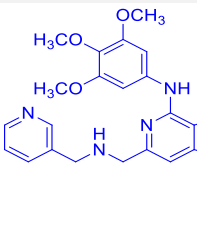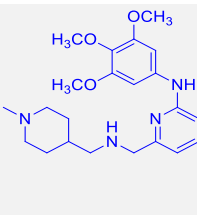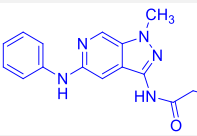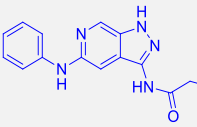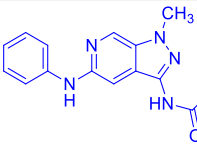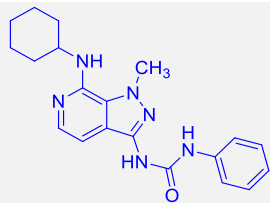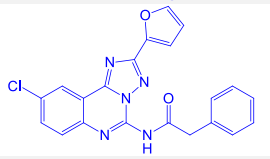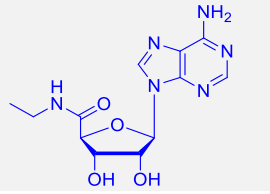
Figure 2. Characterisation of **A15, A17** and **A26** analogues, at the A₃R and A₁R. A₃R Flp-In CHO (top panel) cells or CHO-K1 cells expressing A₁R (bottom panel) were stimulated with 10 μM forskolin varying concentrations of NECA, and either 1 μM potential antagonist (red curves) or DMSO (blue curves- for 30 mins and cAMP accumulation detected. NECA inhibition data were fitted using a three-parameter logistic equation to determine the pIC₅₀ of NECA in each condition; n = 3 independent repeats, each conducted in duplicate. All values are mean ± SEM, expressed as % 100 μM forskolin response.

The data in Figure 2 enables a crude estimation of the potential affinty of each antagonist at the two AR subtypes when analysed using Schild analysis and eq. (1). [63] Based upon a single concentration of antagonist we calculated their affinities constants (pK_d) of each compound (Table 1). Due to their weak activities we used 10 μM of **A26**, **L5** and **L21** for our analysis. Even under these condistions **L21** did not display any activity at the A₁R.

Table 1. Binding affinities measured using BRET or Schild curves and functional activities for **A15**, **A17**, **L2-L10**, and **A26**, **L12**, **L15**, **L21** against A₃R, A₁R.

		A₃R			A₁R		
	COMPOUND	pIC₅₀ in presence of NECA [a]	pK_d [b]	pK_i [c]	pIC₅₀ in presence of NECA [a]	pK_d [b]	pK_i [c]
A15		8.71 ± 0.14	5.91 ± 0.19	5.49 ± 0.10	7.99 ± 0.14	6.91 ± 0.18	6.64 ± 0.08
A17		7.12 ± 0.13	7.87 ± 0.18	8.01 ± 0.06	6.70 ± 0.10	8.25 ± 0.15	8.36 ± 0.10

L2		8.55 ± 0.13	6.26 ± 0.18	6.20 ± 0.06	8.30 ± 0.15	6.54 ± 0.19	6.54 ± 0.07
L3		8.42 ± 0.19	6.45 ± 0.23	6.22 ± 0.10	**8.49 ± 0.17**	**6.28 ± 0.20**	**7.91 ± 0.09**
L4		**7.22 ± 0.09**	**7.77 ± 0.16**	**7.36 ± 0.05**	**7.87 ± 0.10**	**7.04 ± 0.14**	**6.67 ± 0.18**
L5		**7.91 ± 0.10**	**7.05 ± 0.2**	**7.26 ± 0.03**	8.54 ± 0.14	6.20 ± 0.18	6.66 ± 0.14
L6		8.29 ± 0.10	6.60 ± 0.24	7.00 ± 0.10	8.72 ± 0.23	6.84 ± 0.23	6.78 ± 0.30
L7		8.31 ± 0.21	6.59 ± 0.25	6.88 ± 0.08	**7.64 ± 0.14**	**7.29 ± 0.18**	**7.64 ± 0.57**
L8		8.14 ± 0.20	6.80 ± 0.24	7.19 ± 0.10	**8.41 ± 0.22**	**7.18 ± 0.25**	**6.69 ± 0.30**
L9		**8.05 ± 0.10**	**6.89 ± 0.20**	**7.19 ± 0.07**	**7.92 ± 0.11**	**6.99 ± 0.16**	**7.20 ± 0.04**
L10		8.56 ± 0.20	6.24 ± 0.24	6.72 ± 0.09	8.33 ± 0.15	6.50 ± 0.19	6.13 ± 0.08
A26		**7.91 ± 0.19**	**7.05 ±0.22**	**7.07 ± 0.08**	8.58 ± 0.10	6.13 ± 0.17	6.53 ± 0.27
L12		8.52 ± 0.21	6.31± 0.24	6.33 ± 0.09	8.16 ± 0.09	6.71 ± 0.14	6.44 ± 0.11
L15		8.17 ± 0.20	6.77 ± 0.24	6.95 ± 0.08	8.30 ± 0.14	6.54 ± 0.17	6.02 ± 0.14

Compound		A		B		C
L21		8.37 ± 0.19	6.52 ± 0.2	6.60 ± 0.13	8.85 ± 0.12	<6.0	<6.0
MRS 1220		-	10.01 ±[#]	9.94 ±0.11	7.32 ± 0.09	7.62 ± 0.14	7.29 ± 0.27
NECA		9.03 ± 0.13	-	6.63 ± 0.15	8.95 ± 0.10	-	7.08 ± 0.05

[a] Functional activities (pIC$_{50}$ values in presence of NECA) for the ligands as mean ± standard error of the mean (SEM) of at least 3 independent repeats, conducted in duplicate – values obtained from Figure 2.
[b] Dissociation constant (pK$_d$) of the ligands as mean ± standard error of the mean (SEM) of at least 3 independent repeats, conducted in duplicate as determined using the Schild analysis (Equation 1).
[c] Equilibrium binding affinities of the ligands measured with NanoBRET against WT A$_3$R or A$_1$R; NECA was used as positive control as described in ref [20].
[#] Value obtained from ref [20] using IB-MECA as an agonist.

Structural novelty of the compounds as ARs antagonists

The identified pyrazolo[3,4-c]pyridine derivatives provides a novel scaffold for the development of ARs antagonists. Representative nonxanthine pyrazolo derivatives that have been reported as ARs ligands include pyrazolo-[4,3-*e*]-1,2,4-triazolo-[1,5-*c*]pyrimidines, pyrazolo-[3,4-*c*] or -[4,3-*c*]quinolines, pyrazolo-[4,3-*d*]pyrimdinones, pyrazolo-[3,4-*d*]pyrimidines, and pyrazolo-[1,5-*a*]pyridines. [117] Searching in ChEMBL using similarity-based parameters for **A15/A17** or **A26**, ie. the TanimotoCombo [67] coefficient (Tc) with a value > 0.85, we did not find similar compounds or any other pyrazolo[3,4-c]pyridines as ARs antagonists.

Competition binding assays and determination of kinetic parameters of antagonist binding at A$_3$R and A$_1$R using NanoBRET

The using single point antagonist concentrations to determine affinities constants via a Schild analysis is not the most quantitatively accurate method. Thus, we determined the binding affinities for all 15 pyrazolo[3,4-c]pyridines at the A$_3$R and A$_1$R using a BRET-based competition binding assay (Figure 3 and Table 2). We tested the compounds for their ability to displace and inhibit the specific binding of CA200645, [118] a fluorescent antagonist of A$_3$R and A$_1$R, using Nluc-A$_3$R HEK293 and Nluc-A$_1$R expressed in HEK293 cells as we described previously. [20] The NanoBRET binding assay can also enable determination of the kinetics of the compounds binding, which Schild regression does not allow. Indeed, we [20] and others [118] have described the use of NanoBRET binding techniques to determine the real-time kinetics [119,36,35] and affinities of ligand binding at the ARs. Values were derived using the 'kinetics of competitive binding' model build into GraphPad Prism 9.0 enabling determinations of the compounds K$_{on}$ (k_3) and K$_{off}$ (k_4) (Table 2). The reciprocal of the K$_{off}$ enables a determination of the residence time (RT) of a compound. [20] Beyond this, we also determined the pK$_d$ of the compounds (k_4/k_3) from the kinetics assays and compared these values to those determined from the saturation binding assays and the Schild analysis.

The kinetic parameters for CA200645 binding at the Nluc-A$_3$R were determined as K$_{on}$ (k_1) = 2.86± 0.45 x 10^6 M^{-1} min^{-1}, K$_{off}$ (k_2) = 0.064 ±0.0023 min^{-1} with a K_d = 25 ± 4.6nM. Conversely the kinetics of binding for CA200645 binding at the Nluc-A$_1$R were determined as K$_{on}$ (k_1) = 3.67 ± 0.34 x 10^6 M^{-1} min^{-1}, K$_{off}$ (k_2) = 0.067 ±0.005 min^{-1} with a K_d = 18.29 ± 2.4 nM. Using these parameters, we were able to provide estimates of the kinetics of binding for most of the **A17** and **A26**-based derivatives with exception of **A15**, **L2**, **L3**, **L8**, **L15** and **L21** at the A$_3$R and **L21** at the A$_1$R which failed to provide a reliable fit to the data, likely due to their high K_d values (Table 2).
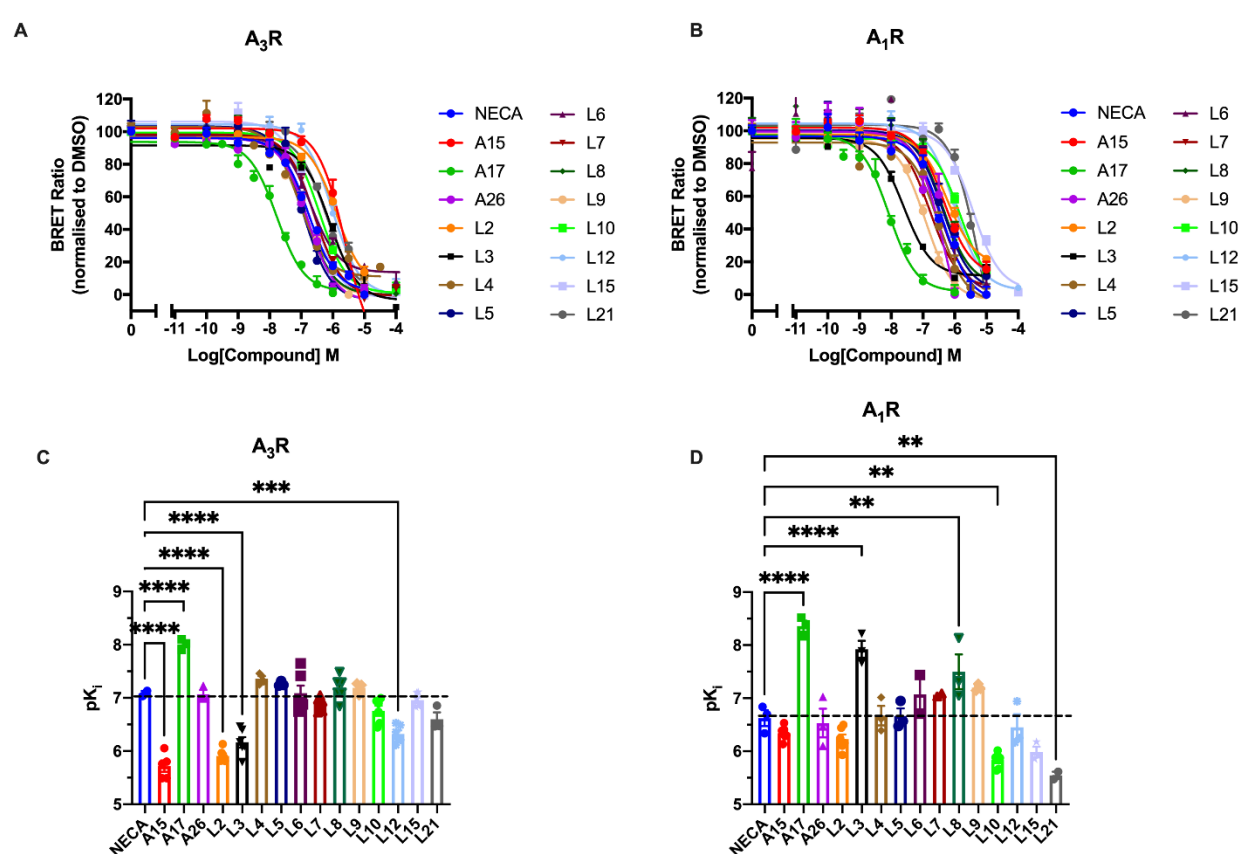
Figure 3. Inhibition of BRET between Nluc and CA200645 at the A_3R and A_1R by **A17** and **A26** and their derivatives. HEK293 cells expressing Nluc-A_3R (**A**) or Nluc-A_1R (**B**) were treated with 5 nM or 20 nM CA200645, respectively enabling concentration-dependent decreases in BRET ratio at 10 min to be determined with the response normalised to DMSO. Binding curves were fitted with the Cheng Prusoff equation built into Prism to enable estimates of the pK_i. Comparison of pK_i values for the A_3R (**C**) and A_1R (**D**) as determined via BRET binding. Dash line represents the mean pK_i value of NECA for comparison. Each data point represents mean ± SEM of at least 3 experiments performed in duplicate.

Many of the compounds showed a good agreement between the different methods used to determine their affinities as compared in Table 1 and Table 2. Thus, consistent with the Schild analysis compound **A17** displayed the highest affinity at the A_3R followed by **L4>L6=L5=A26=L9**. At A_1R **A17** also had the highest affinity with the rank order of affinities being **A17>L3>L9>L7>L4**. All the other compounds displayed weaker affinities. Comparison of the affinity constants calculated by the NanoBRET binding assays and the single dose Schild analysis once again showed close agreement except for compound **L3** at the A_1R where the affinities determined in the BRET binding assays for were 50-fold higher than in the Schild analysis. This may indicate that **L3** has unusual properties compared to the other compounds tested here.

From this data we observed that the most interesting potencies at 1 µM concentration (indicated in bold in Table 1) include: (a) **L3** or **L4**, **L5**, **L7,L8**, **L9**, **A17**, which are pyrazolo-[3,4-c]pyridines with isopropyl or phenyl group at 3-position, respectively, a cyano or chloro or aminomethyl or N-(arylmethyl)aminomethyl group at 5-position and an anilino group at 7-position, (b) **A26**, which is 3-acetamido-5-anilino pyrazolo-[3,4-c]pyridine. The affinities range for **A17** series including compounds **L2-L10**, **A15** was between low micromolar to low nanomolar. The affinities range for **A26** series including compounds **L12**, **L15**, **L21** was between low micromolar to 100 nM.

Table 2 Kinetics of binding for the **A17**- and **A26**-panels of compounds to the orthosteric binding area at the A_3R and A_1R.

COMPOUND	A_3R				A_1R			
	Kon (k_3) x10^5 M^-1 [a]	Koff (k_4) min^-1 [b]	pK_d Kinetics [c]	RT (mins) [d]	Kon (k_3) x10^5 M^-1 [a]	Koff (k_4) min^-1 [b]	pK_d Kinetics [c]	RT (mins) [d]
A15	<50	<0.4	N.D.	>2	3.18 ±1.0	0.03 ±0.006	6.99 ±0.21	38.7 ±8.8
A17	21.3 ±1.2	0.021 ±0.003	8.00 ±0.32	47.23± 8.2	139.7 ±1.5	0.024 ±0.009	8.76 ±0.07	41.31 ±4.56
L2	<50	<0.4	N.D.	>2	1.72 ±0.3	0.048 ±0.01	6.55 ±0.03	22.9 ±4.3
L3	<50	<0.4	N.D.	>2	45.07 ±3.4	0.061 ±0.002	7.86 ±0.45	16.3 ±0.3

L4	8.2 ±0.5	0.026 ±0.006	7.58 ±0.32	46.72 ±4.5	11.5 ±4.0	0.051 ±0.004	7.21 ±0.51	20.61 ±3.4
L5	3.65 ±0.6	0.031 ±0.01	7.07 ±0.22	32.05 ±6.3	2.79 ±0.29	0.055 ±0.001	6.70 ±0.54	18.2 ±4.37
L6	24.7 ±3.8	0.18 ±0.02	7.13 ±0.55	5.55 ±2.6	5.23 ±0.45	0.036 ±0.005	6.88 ±0.23	27.72 ±3.7
L7	4.8 ±2.4	0.105 ±0.04	6.59 ±0.73	9.55 ±3.5	9.63 ±2.5	0.039 ±0.004	7.39 ±0.40	25.34 ±4.9
L8	<50	<0.4	N.D	>2	2.34 ±0.6	0.054 ±0.005	6.37 ±0.11	18.50 ±2.6
L9	5.62 ±1.0	0.054 ±0.02	7.0 ±0.33	17.85 ±4.3	8.17 ±1.4	0.02 ±0.015	7.54 ±0.10	43.96 ±2.1
L10	3.38 ±1.1	0.01 ±0.001	6.56 ±0.43	10.85 ±3.4	1.65 ±0.4	0.04 ±0.007	6.64 ±0.03	31.43 ±7.1
A26	12.45 ±1.8	0.096 ±0.03	7.11 ±0.45	10.4±3.4	3.36 ±1.6	0.134 ±0.003	6.40 ±0.18	7.47 ±2.2
L12	1.45 ±0.3	0.051 ±0.03	6.45 ±0.22	19.04 ±5.6	1.84 ±0.4	0.052 ±0.003	6.55 ±0.40	19.23 ±4.5
L15	<50	<0.4	N.D.	>2	0.834 ±0.3	0.071 ±0.004	6.07 ±0.22	14.06 ±2.4
L21	<50	<0.4	N.D	>2	<50	<0.4	ND	>2
MRS1220	3250± 2.8[#]	0.025 0.005[#]	10.11[#]	40.32[#]	14.54±0.4	0.023 ±0.0008	7.80 ±0.2	43.67 ±5.6

[a] K_{on} (k_3) for ligands as determined using NanoBRET binding assays using either Nluc-A_3R or Nluc-A_1R expressing HEK 293 cells and determined through fitting with the 'Kinetics of competitive binding' model.

[b] K_{off} (k_4) for ligands determined as in a.

[c] Kinetic dissociation constant (pK_d) for each ligand as determined from K_{on}/K_{off}.

[d] Residence time of each ligand as determined by the reciprocal of the K_{off}.

[#] Value obtained from ref [20].

Note – values in red could not be fitted using the 'kinetics of competitive binding' model.

Using all these methods to determine antagonist affinities suggests that **A17**, **L4** displayed low nanomolar affinities and **A26**, **L5**, **L8**, **L9** mid-nanomolar affinities to the A_3R while the other compounds showed weaker affinities. At the A_1R, only **A17**, displayed low nanomolar affinity and the five compounds **L4**, **L6**-**L9** displayed mid-nanomolar to low nanomolar affinities. Thus, we can conclude that **L4**, **L5** and **A26** displayed selectivity for the A_3R, and **A17**, **L7**, **L8** are A_1R selective compounds compounds (Table 1). Further investigation of the structure-affinity/activity relationships will be discussed in the MD simulations section.

For compounds which displayed high affinity at the A_3R, ie. **A17**, **L4**, **L5** have RT = 35-50 mins while in **L9**, **A26** have RT =10-17 mins. Compounds which displayed high affinity at the A_1R, have RT = 40-50 mins (**A17**, **L9**) or RT = 16-27 min (**L4**, **L5-L8**). To increase the binding affinity of the tested compounds by 10-fold, either the K_{on} should be increased or the K_{off} should be reduced by 10-fold.

Binding profile of the novel pyrazolo[3,4-c]pyridines using MD simulations, MM-GBSA binding free energy calculations and mutagenesis experiments

MD simulations

We performed unrestrained MD simulations and MM-GBSA binding free energy calculations for the antagonists shown in Table 1 to investigate their binding profile to A_1R and A_3R. We carried out the molecular docking calculations of these compounds into the orthosteric site of the A_1R or A_3R using the ChemScore as the scoring function. [2,69] The highest score docking pose was embedded in 12 Å hydrated POPE lipid buffer and the system was subjected to 100ns-MD simulations with the amber ff99sb [75] force field. The MD simulations converged during 100-ns of production (Figure S5). Detailed comparison is discussed between the most potent compound **A17** and congeners in the same series.

***A17** in A_1R.* The MD simulations showed significant interactions (> 20% frequency) of **A17** with E170[5.28], F171[5.29], E172[5.30], M180[5.38], W247[6.48], L250[6.51], H251[6.52], N254[6.55] T270[7.35], Y271[7.36] (Figure 4,A). The simulations showed that **A17** translocates inside the binding area of A_1R from the starting docking pose (Figure 4,A, see also $RMSD_{lig}$ values in Table S5) in order to form more stabilizing hydrogen bonds in addition to the stabilizing hydrophobic and π-π interactions. It has been discussed that the MD simulations in many cases improve the ligand's pose inside the

binding area produced by docking calculations, especially when the binding area is highly flexible and broad. [120,121]

In particular, **A17**-A_1R complex is stabilized by (a) direct hydrogen bonding interactions between both the pyrazole 1-NH and anilino amino groups of the ligands and the amide side chain carbonyl of N250[6.55]; between the pyrazole nitrogen of the ligand and L250[6.51] main chain NH group, (b) water mediated hydrogen bonding interactions between the ligand N-H donor groups and the carboxylate side chain of E172[5.30] or the amide side chain of N250[6.55]; between the ligand oxygen atoms of methoxy groups and E170[5.28] carboxylate or Y271[7.36] hydroxyl group; between the 3-cyano group of the ligand and W(6.48), Y(7.36). (c) hydrogen bonds between the cyano group of the ligand with waters that are inserted in the region between the ligand and TM1-TM2 (Figure 4,A). (d) Significant π-π stacking interactions are formed between the core pyrazolo-[3,4-c]pyridine scaffold and the F171[5.29] side chain phenyl and between the ligand phenyl substituent and the imidazole of H251[6.52] or indole of W247[6.48]. Hydrophobic interactions are formed between the trimethoxy-phenyl group of the ligand, which is directed either towards the water exposed area of the receptor or to EL2, and Y271[7.36]; between the pyrazole ring of the ligand and M180[5.38], L246[6.51]; between the phenyl ring of the ligand, which is oriented deeper into the receptor from the pyrazole scaffold, and W243[6.48].
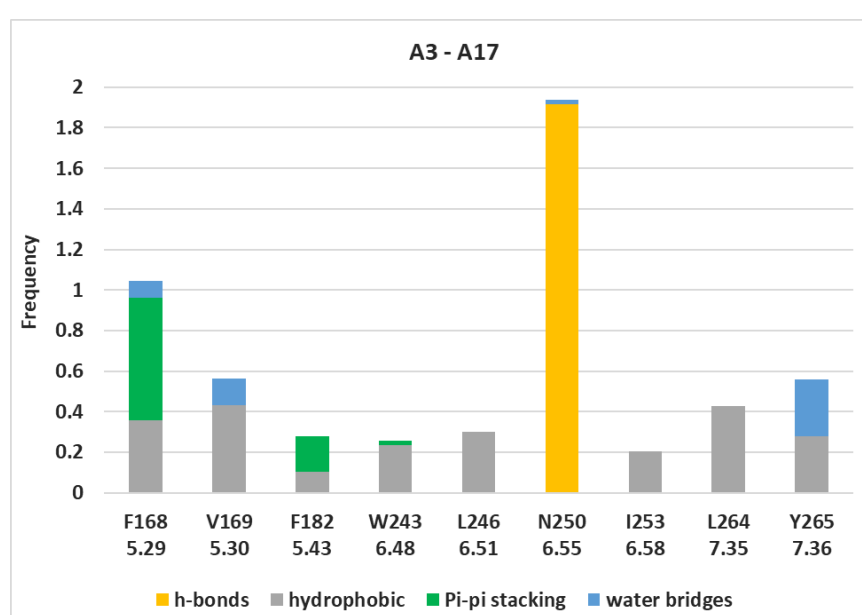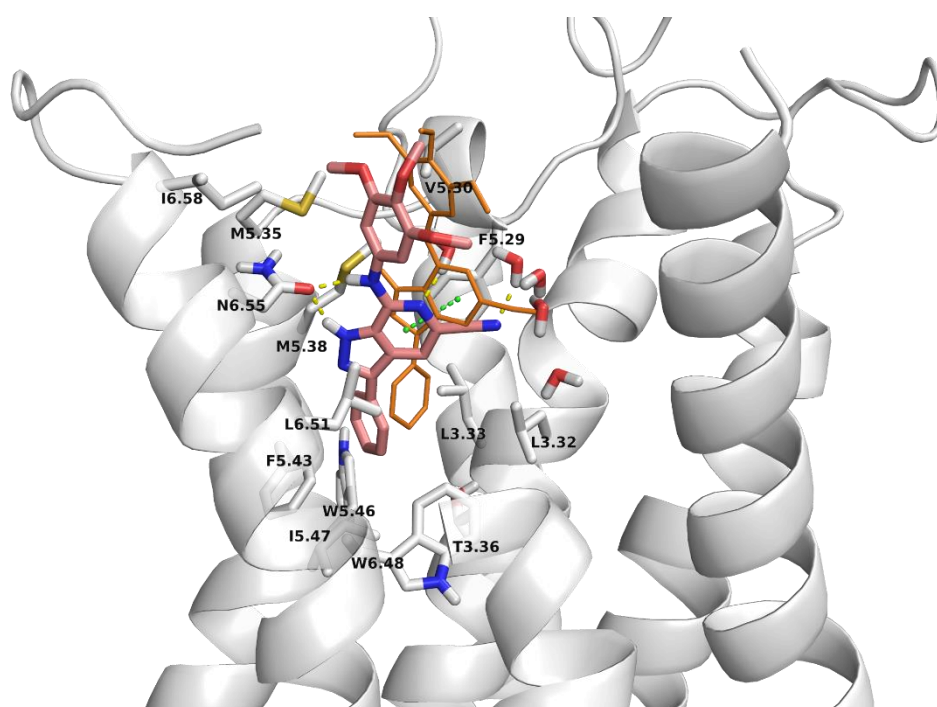
(A)
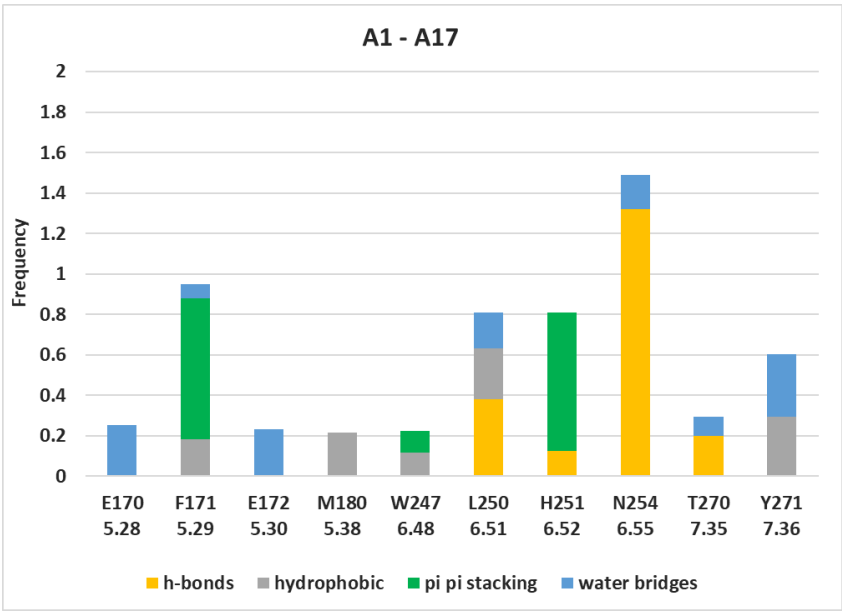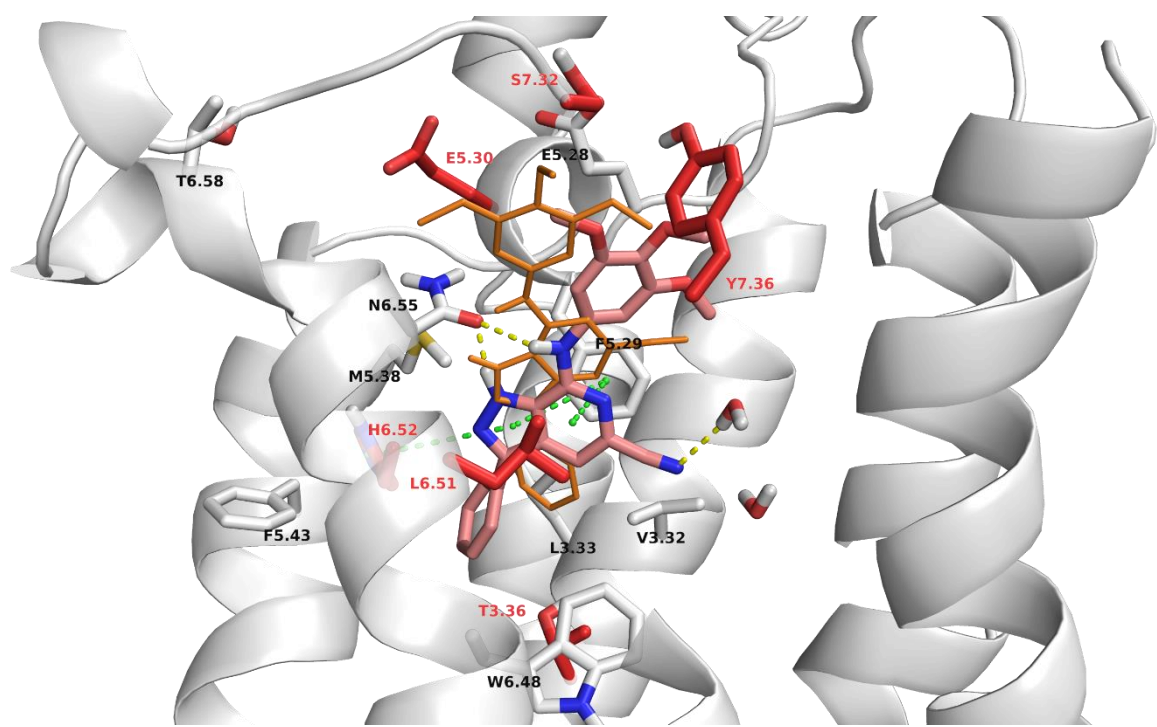
(B)

Figure 4. Representative frames of **A17** and receptor-ligand interaction frequency histogram inside the orthosteric binding area of WT A_1R (A), A_3R (B) from 100ns-MD simulations. Bars are plotted only for residues with interaction frequencies ≥ 0.2. Color scheme: Ligand=pink sticks, ligand's starting position=orange wire, receptor=white cartoon and sticks, hydrogen bonding interactions=yellow (dashes or bars), π-π interactions=green (dashes or bars); hydrophobic interactions=grey; water bridges-blue. Mutagenesis experiments were performed for A_1R with point mutations to alanine of residues shown in red sticks and/or noted in red color in the frame shown in (A). For the protein models of A_1R or A_3R were used the experimental structure of the inactive form for A_1R (PDB ID 5UEN [122]) or A_2AR (PDB ID 3EML[5]) in complex with an antagonist.

A17 in A_3R. The 100 ns-MD simulation of **A17** inside the orthosteric binding site of A_3R revealed that compound **A17** also translocates from its starting docking pose inside the binding area (Figure 4,B). The MD simulations showed that the NH-(p-trimethoxy)-phenyl group of **A17** is oriented towards the water exposed area of the receptor, where form hydrophobic interactions with $V169^{5.30}$, $M174^{5.35}$, $I253^{6.58}$, $L264^{7.35}$, $Y265^{7.36}$.

It is worth note that this trimethoxy-anilino orients towards the extracellular region in both A_1R and A_3R. However, while this group enters in A_3R between TM5, TM6 where it is stabilized with hydrophobic forces with $V169^{5.30}$, $M174^{5.35}$, $I253^{6.58}$ in A_1R is positioned between TM3-TM5 to avoid repulsions with $E172^{5.30}$. We observed similar results before when we observed that IB-MECA binds similarly to A_3R and $V169^{5.30}E$ A_3R. [21] More elaborated modifications [123] are needed to take advance of the difference in position 5.30 between A_3R and A_1R or A_2AR receptors due to the high similarity but also broadness and plasticity of their orthosteric binding area that enables ligands with flexible substituents to change accordingly their binding pose to fit into the binding site.

The nitrogen aromatic ring is engaged in aromatic π-π stacking interaction with the phenyl group of F168[5.29] and hydrophobic interactions with L246[6.51] (Figure 4,B). The phenyl ring is oriented deeper into the receptor where it forms London dispersion interactions with F182[5.43], W243[6.48] and slightly with L91[3.32]. Hydrogen bonding intera ctions are formed between the amide side chain carbonyl of N250[6.55] and the 1-pyrazole NH or anilino NH groups. Again the presence of the polar cyano group is directed towards TM1 – TM2 helices allowing waters to enter the space between the ligand and these TM α-helices (Figure 4,B).

L4-L7 *in A₁R or A₃R.* **L4-L7** contain the basic 3-phenyl-5-substituted-7-anilino pyrazolo[3,4-c]pyridine skeleton and the substituent changes at 7- and 5-position, with no trimethoxy groups at 7-anilino and a Cl, H, aminomethyl, respectively. These substituent changes can have significant changes in binding affinity and functional activity. As shown in Table 1, compared to the low nanomolar antagonist **A17** (pK_d = 8.25) for A₁R and (pK_d= 7.87) for A₃R, in **L6** the 5-cyano group is missing resulting in reduction of binding affinity and functional activity by ca. 100-fold (pK_d = 6.84) against A₁R or ca. 10-fold against A₃R (pK_d = 6.60). Similarly, when the cyano in **A17** is changed to chlorine group in **L5** we observed again ca. 100-fold reduction in affinity for A₁R (pK_d = 6.20) and a 5-fold reduction for A₃R (pK_d = 7.05).

The MD simulations showed that in **A17** the cyano group can be stabilized through waters mediated hydrogen bonding interactions, with waters entering the region between the ligand and TM1, TM2, with residues W(6.48), Y(7.36). The MD simulation trajectories showed that compounds **L6, L5** almost escaped from the orthosteric binding area in A₁R and loose the critical for binding and functional activity interactions between the ligand and residues F(5.29), L(6.51), H(6.52), N(6.55) M(5.35) or M(5.38) are considerably weakened and the interactions with W(6.48), L(7.35), Y(7.36) are vanished (Figure S3).

L4, L7 remained stable inside the orthosteric binding area of A₃R and A₁R during the MD simulation (Figure S3). **L7** has a 5-aminomethyl group instead of 5-cyano group in **A17** resulting in ca 10-fold reduction for A₁R (pK_d = 7.29) and 20-fold reduction for A₃R (pK_d = 6.59). **L4** lacks the trimethoxy substitution of 7-anilino group and this results in 10-fold reduction in affinity for A₁R (pK_d = 7.04) but maintenance for A₃R (pK_d = 7.77).

The effect of the 5-ammonium group in the binding mode was remarkable. The 100ns-MD simulations showed that **L7** in A₁R compared to **A17** can interact with F171[5.29], W247[6.48] but is inclined towards TM3, TM7 and moves deeper in the binding area due to the presence of the protonated 5-aminomethyl group which is attracted strongly by H278[7.43], losing the direct hydrogen bonding interactions with N254[6.55]/E172[5.30] and hydrophobic contacts with M180[5.38], L250[6.51]. Thus, the ligand forms direct hydrogen bonds mainly to H278[7.43] and waters mediated hydrogen bonds with T277[7.42], E172[5.30], N184[5.42] and van der Waals contacts with TM3 residues V87[3.32], T91[3.36] and TM7 residue I274[7.39] (Figure S3). A similar behaviour was observed also **for** L7 inside A₃R.

L8, L9 *in A₁R or A₃R.* Compounds **L8** or **L9** have a phenylmethyl or 3-(pyridinyl)methyl group connected with the 5-aminomethyl group of compound **L7** which compared to **A17** binds deeper in the binding area as previously discussed. The MD simulations showed that compounds L8, L9 are stabilized inside the binding area. Compared to **A17**, **L8** adopts the same position and binding interactions, ie. with residues F171[5.29], E172[5.30], M180[5.38], W247[6.48], L250[6.51], N254[6.55] inside the orthosteric binding area of A₁R, A₃R. The binding and pharmacological data showed that **L9** (pK_d = 6.89) for A₃R and (pK_d = 6.99) for A₁R is almost equipotent to L8 and has 10-fold smaller binding affinity compared to **A17** against A₁R, A₃R (Table 1). **L9** ligand in A₁R forms hydrogen bonding interactions through the ammonium group in 5-aminomethyl moiety with H278[7.43] and hydrophobic contacts through its pyridinylmethyl group with V62[2.57], A66[2.61], V87[3.32] and I274[7.39]. Similarly, **L8** showed contacts with A66[2.61] (Figure S3). These contacts are favoured due to the stabilization of the pyridinylmethyl or benzyl group close to TM2, TM3. Compared to A₁R, A₃R has a narrower binding area and V169[5.30] instead of E172[5.30] so the pyrazolo[3,4-c]pyridine ring is tilted, and the N-CH₂Ar bond is rotated to make contacts with TM1 while the ammonium group of 5-aminomethyl moiety can be hydrogen bonded with E172[5.30]. It is worth to note that compounds **L8, L9** have contacts through all their fragments with A₁R or A₃R and are extended inside the binding area from TM6 to TM2 (Figure 5A,D). (Results for **L10** and **L26** are described in the Supporting Information).
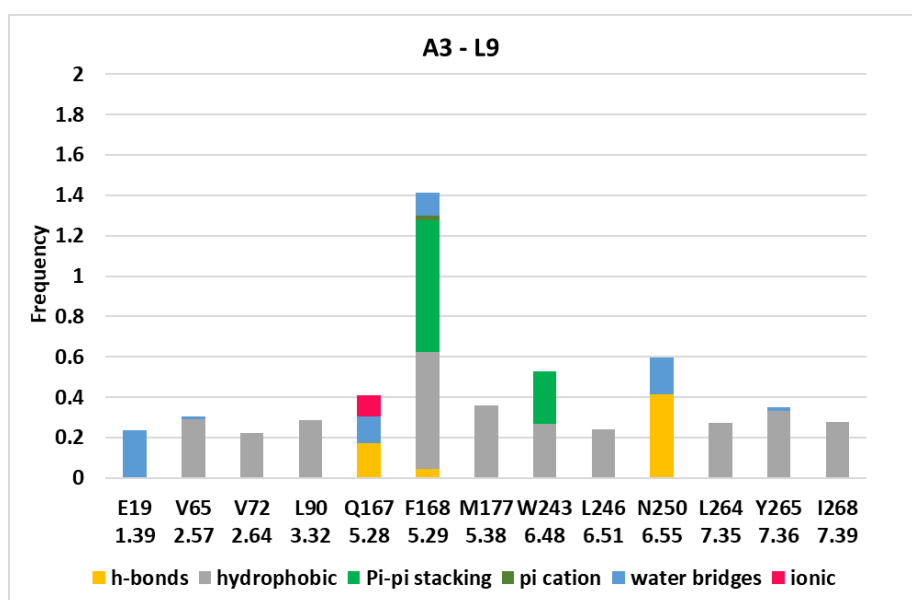
(A)
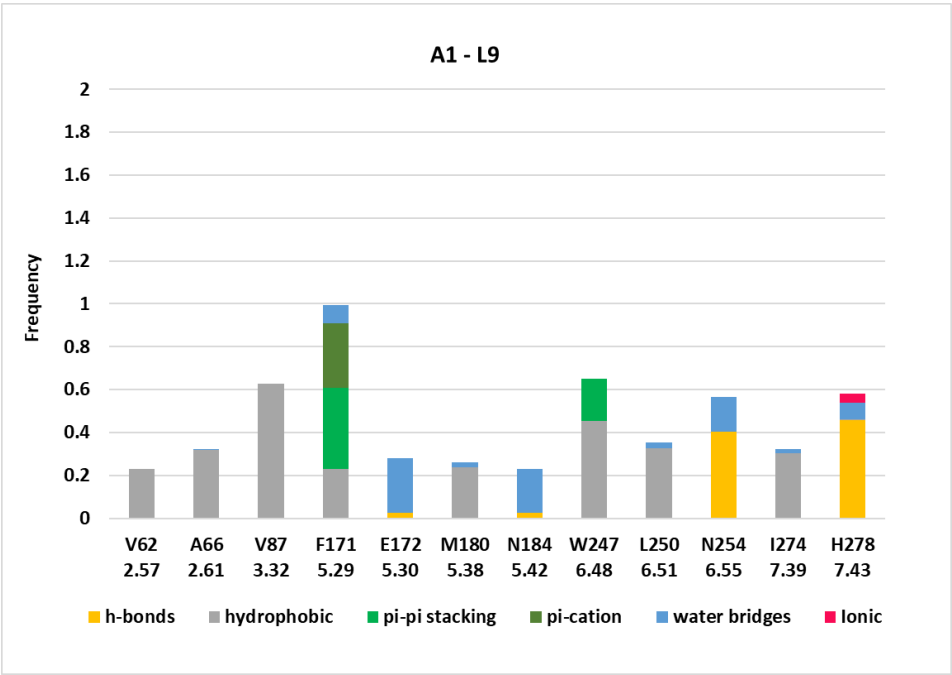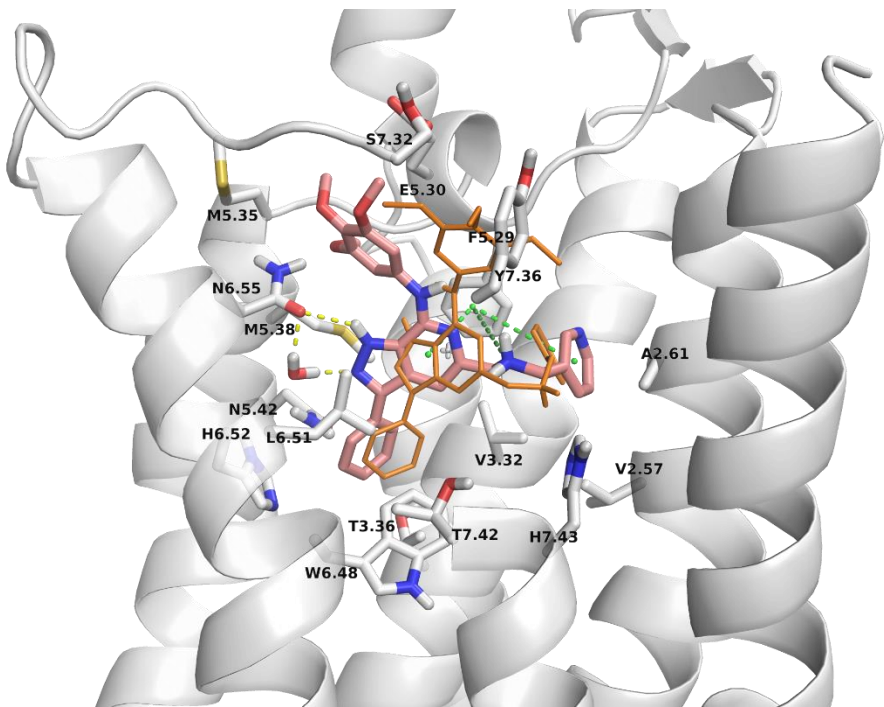
(B)
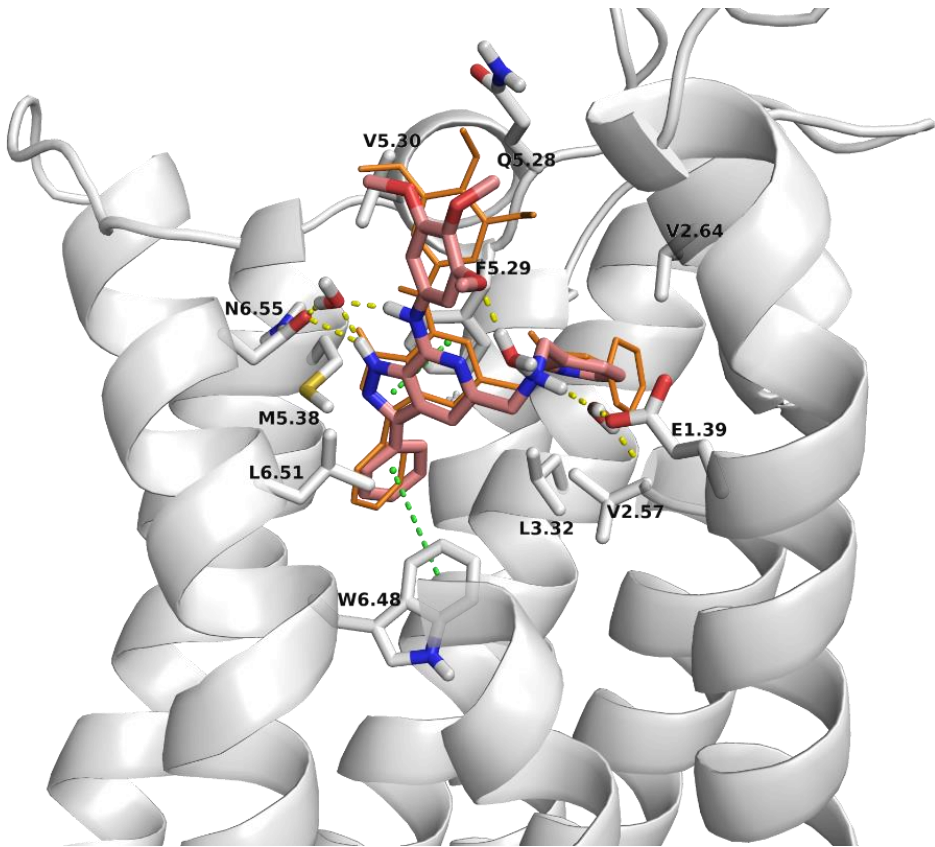
Figure 5. (A),(B)(top) Representative frames of **L9** and receptor-ligand interaction frequency histogram inside the orthosteric binding area of WT A_1R (A), A_3R (B) from 100ns-MD simulations. Bars are plotted only for residues with interaction frequencies ≥ 0.2. Color scheme: Ligand=pink sticks, ligand's starting position=orange wire, receptor=white cartoon and sticks, hydrogen bonding interactions=yellow (dashes or bars), π-π interactions=green (dashes or bars); hydrophobic interactions=grey; water bridges-blue. For the protein models of A_1R or A_3R were used the experimental structure of the inactive form for A_1R (PDB ID 5UEN [122]) or A_2R (PDB ID 3EML[5]) in complex with an antagonist.

MM-GBSA calculations

A post processing analysis of the MD simulations of the tested compounds **A15, L2-L10, A17, L12, L15, L21, A26** in complex with A_1R or A_3R was applied with the MM-GBSA method and the OPLS2005 [82,83] force field using a hydrophobic slab as implicit membrane model and including waters in the orthosteric binding area, in a radius of 4 Å from the center of mass of the ligand. [55,86] Compared to the most potent compound **A17** the MM-GBSA calculations showed correctly that the deletion of a group or substituent in **A17** results in much more positive ΔG_{eff} values, ie. lower binding affinities. However, the MM-GBSA method can't predict the direction in free energy change by changing a substituent to another one for example replacing the 5-choro in **L5** by the 5-cyano at A17 (see discussion in the Supporting Information, Table S5, Figure S6). However, such accuracy is possible for perturbation methods based on statistical mechanics.

Mutagenesis experiments

We confirmed in a previous publication, [20–22] for the selective A_3R antagonist **K18** that mutation of residues V169[5.30], M177[5.38], L246[6.51], F168[5.29], N250[6.55] to alanine caused a reduction or negation of activity as has been described previously. [20–22] Indeed, residues F(5.29), M(5.38), L(6.51), N(6.55) interact directly with all AR ligands, according to the resolved X-ray structures for A_2R [5–9] and A_1R [10,11] or MD simulations. [21,22,123–125] Thus, their mutation to alanine caused a reduction or negation of functional activity for all agonists or antagonists against all ARs. [126–131]

Here, we focused on A_1R, and we investigated experimentally residues that are important for the binding of **A17** and **A26** to A_1R (in comparison to NECA) using mutagenesis and binding affinity assays measured using the NanoBRET method. [20] Mutagenesis experiments were performed for A_1R with point mutations to alanine of residues shown in red sticks and/or noted in red color in the MD simulations frame shown in Figure 4,A. The selection of these residues which are embraced by the ligand was guided by the MD simulations of the complex of A_1R with the most potent ligand **A17**. Initially we determined the affinity constant for CA200645 at each of the A_1R mutants T91[3.36]A, E172[5.3]A, L250[6.54]A, H251[6.52]A all disapplying reduced affinity for the fluorescent tracer. Mutation of S267[7.32] and especially of L250[6.51] to alanine significantly increased the affinity of **A17**. This was unusual since L[6.51] is key-to-recognition and highly conserved residue in all four AR subtypes. [20,19] Consistent with previous findings, the mutation S267[7.32]A [126] also increased significantly the binding affinity of NECA to the A_1R. Interestingly, mutation of E172[5.30] or Y271[7.36] to alanine both significantly reduced the binding affinity of NECA but had little effect upon **A17** or **A26** affinity.

Table 3. Binding affinities (K_d's) for **NECA**, **A17** and **A26** measured using NanoBRET against WT A$_1$R and mutant A$_1$Rs.

Mutation	K_d (nM) [a]	A17	A26	NECA
WT	76.37 ± 9.37	7.87 ± 0.06	6.30 ± 0.07	6.67 ± 0.05
T91$^{3.36}$A	166.35 ± 17.36	8.37 ± 0.07 **	6.10 ± 0.07	n.b. [b]
E172$^{5.30}$A	116.04 ± 12.22	7.63 ± 0.08	5.98 ± 0.06	5.38 ± 0.06 **
L250$^{6.51}$A	158.28 ± 17.37	8.44 ± 0.05 **	6.15 ± 0.09	n.b. [a]
H251$^{6.52}$A	145.19 ± 19.13	8.03 ± 0.10*	7.15 ± 0.08**	8.04 ± 0.10 **
S267$^{7.32}$A	70.99 ± 7.03	8.10 ± 0.16 **	5.97 ± 0.17	6.31 ± 0.10
Y271$^{7.36}$A	71.10 ± 7.68	7.82 ± 0.04	6.33 ± 0.07	5.45 ± 0.06 **

[a] Affinity constant for CA200645 binding to mutant A$_1$R receptors.
[b] n.b. NECA was unable to displace CA200645 at the mutant receptor
Statistical significance (* $p < 0.05$, ** $p < 0.01$,) determined using ANOVA and Dunnett' s post-test.

We observed [139] that residues lying 4>Å apart from the ligand can significantly influence binding through allosteric interactions, as we [20,21,22] and others groups [126,129] showed. Indeed, deeper in the orthosteric binding pocket residues H(7.43), T(3.36), S(7.42) and often H(6.52) are important for hydrogen bonding interactions with ribose of ARs agonists. Mutations T(3.36)A [133] and S(7.42)A [86] reduced agonist potency at A$_{2A}$R and A$_1$R but can have a negligible effect or can increase potency of partial agonists or antagonists at A$_1$R, [126,129] or A$_{2A}$R, [126,127,129–131] respectively. [126,129] H(6.52) stabilizes both agonists and antagonists, through interaction with the different modifications emerging from the core scaffold. H(7.43) and H(6.52) mutations to alanine strongly reduced agonist and antagonist potency against A$_{2A}$R. [128,129] The effect of H(6.52)A mutation is usually the same observed for antagonists against A$_3$R [20–22,126] or other antagonists against A$_1$R. This is in line with the abolished agonist and antagonist A$_{2A}$R binding observed in the H251$^{6.52}$A mutant, [128,129] while mutation to a bulky phenyl alanine did not significantly affect antagonist binding. [129,134] The A$_3$R has a serine in this position, which might explain why it is more tolerant towards larger substituents binding deep in the pocket.

We were unable to determine any binding for NECA at T91$^{3.36}$A mutant in agreement to similar observations for A$_{2A}$R [135] since, as we suggested previously for A$_3$R, NECA binds to the orthosteric binding area through hydrogen bonding also to T91$^{3.36}$. [21] Mutation T91$^{3.36}$A increased the affinity for **A17** as reported previously for A$_{2A}$R and antagonist LUF5834, [127] while displaying no significant effect for **A26.** Mutation H251$^{6.52}$ to alanine also significantly increased the affinity of **A17**. This confirmed the allosteric participation of T91$^{3.36}$, H251$^{6.52}$, which although are deep in the binding pocket, contribute in the stability of the binding interactions of A17 (Table 3). For **A26**, only mutation of H251$^{6.52}$ resulted in any appreciable increase in affinity. Consistent with previous findings, mutations S267$^{7.32}$A, H251$^{6.52}$A [126] also increased significantly NECAs affinity to the A$_1$R.

TI/MD relative binding free energy calculations

The FEP/MD [136] and TI/MD [89,90] methods can provide accurate results for relative binding free energies with a method error 1 kcal mol^{-1}. They have been applied for ligands optimization in class A GPCRs [57,123,137–139] including ARs [123,138] and may be also used successfully in cases where an homology model is only available. [140]

We performed TI/MD calculations for the set of 9 alchemical transformations shown in Table 3 for a set of compounds that have Kd's differing in a range of ca. 100 units. Generally, we carried out the calculations using the 1-step protocol which changes the charges and van der Waals interactions in a single simulation by activating both Lennard-Jones and Coulomb softcore potentials simultaneously, reducing the computational cost (see also description in Methods section). We obtained (a) relative binding free energy values that were quite close to the experimental values with deviations being in most of the cases < 1 kcal mol^{-1}, ie. within the accuracy of the method (mue = 1.03 kcal mol^{-1} or 0.96 kcal mol^{-1} for A$_1$R and A$_3$R. respectively, see Table 3); (b) a strong spearman rank correlation p = 0.82 or 0.84 (Figure 7) for the alchemical transformations of A$_1$R-or A$_3$R-complexes, respectivey, suggesting that the binding sites used are reliable and the TI/MD calculations describe accurately the binding interactions and can be used for structure-based drug design. [57,123,137–139] The TI/MD simulations can calculate accurately the changes in binding affinity between different substituents that we have already described in MD simulations section qualitatively using protein-ligand interactions frequency plots combined with RMSD$_{lig}$ values as descriptors.

Table 3. Relative binding free energies computed by TI/MD calculations ($\Delta\Delta G_{b,TI/MD}$ in kcal mol^{-1}) using alchemical transformations and a thermodynamic cycle and measured experimentally ($\Delta\Delta G_{b,exp}$ in kcal mol^{-1}) for pairs of compounds complexed to A$_1$R or A$_3$R.

A$_1$R	$\Delta\Delta G_{B,TI/MD}$	$\Delta\Delta G_{B,EXP}$ [a]	$\|\Delta\Delta G_{B,TI/MD}- \Delta\Delta G_{B,EXP}\|$ [b]
A15 → L3	-0.66 ± 0.07	-1.80 ± 0.09	1.14
A15 → A17	-1.06 ± 0.09	2.44 ± 0.09	1.38
L3 → A17	-0.87 ± 0.09	-0.63 ± 0.09	0.24
L4 → A17	-3.34 ± 0.1	-2.39 ± 0.15	0.95
L6 → A17	-3.05 ± 0.05	-2.24 ± 0.20	0.81
L6 → L5	-0.67 ± 0.04	0.16 ± 0.22	0.83
L9 → L8	0.71 ± 0.08	0.72 ± 0.17	0.01
L12 → A26	1.66 ± 0.06	-0.13 ± 0.19	1.79
L15 → A26	1.37 ± 0.12	-0.72 ± 0.21	2.09

A$_3$R	$\Delta\Delta G_{B,TI/MD}$	$\Delta\Delta G_{B,EXP}$ [a]	$\|\Delta\Delta G_{B,TI/MD}- \Delta\Delta G_{B,EXP}\|$ [c]
A15 → L3	-2.41 ± 0.07	-0.45 ± 0.11	1.96
A15 → A17	-4.07 ± 0.09	-2.99 ± 0.08	1.08
A17 → L3	1.88 ± 0.09	2.54 ± 0.08	0.66
L4 → A17	-1.66 ± 0.07	-0.92 ± 0.06	0.73
L6 → A17	-0.5 ± 0.05	-1.43 ± 0.08	0.93
L6 → L5	-1.32 + 0.04	-0.37 ± 0.06	0.95
L9 → L8	0.99 ± 0.10	-0.004 ± 0.08	0.99
L12 → A26	-1.54 ± 0.05	-1.05 ± 0.09	0.49
L15 → A26	0.68 ± 0.14	-0.17 ± 0.09	0.85

[a] Experimental relative binding free energies ($\Delta\Delta G_{b,exp}$) were estimated using the experimental binding affinities pK_d (Table 1) according to eq. (2) in Methods Section; [b] mue = 1.03 kcal mol^{-1}; [c] mue = 0.96 kcal mol^{-1}

A$_1$R

p = 0.82
mue = 1.03 kcal mol^{-1}
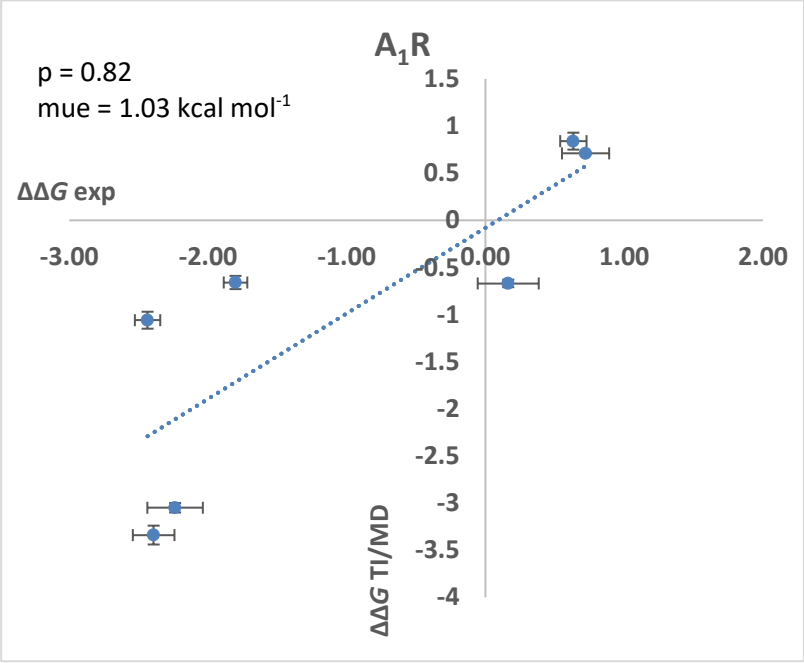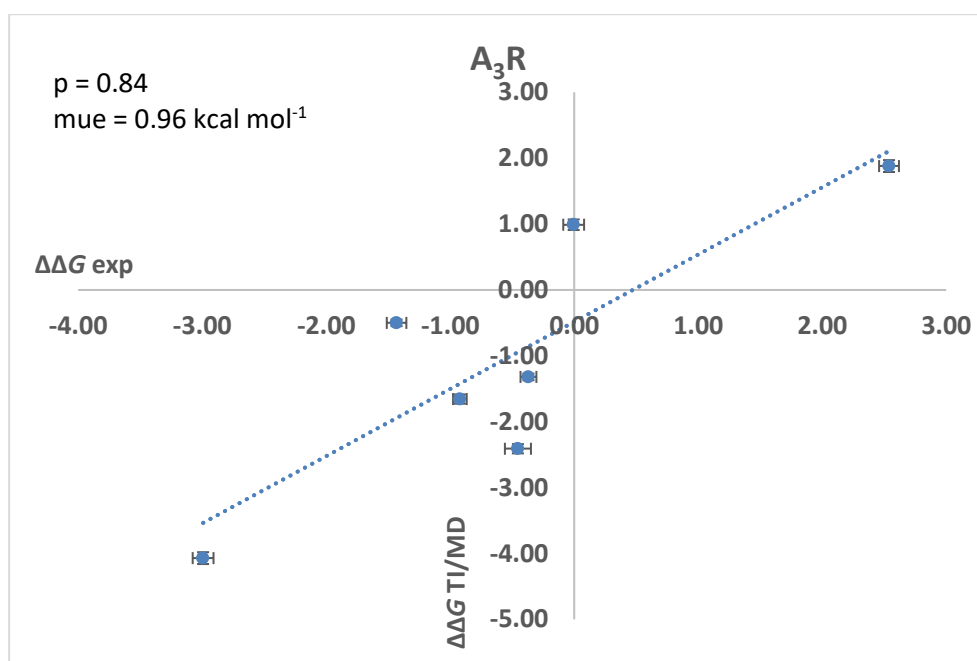
Figure 7. $\Delta\Delta G_{b,bind}$ values computed by TI/MD calculations plotted against $\Delta\Delta G_{b,exp}$ values estimated by the experimental binding affinities pK_d (Table 1) for A_1R and A_3R.

Discussion

We, [19] and other groups, [12–18] are motivated to identify new hits from virtual screening of ARs [19,22] and modify them to lead compounds. However, the possibility of re-purposing compounds from *in-house* libraries [15] is an exciting opportunity and cost-effective process. We identified here the pyrazolo[3,4-c]pyridines **L2-L10, A15, A17** with a phenyl or isopropyl group at 3-position, an anilino group at 7-position and a cyano-, or chloro- or aminomethyl group or N-(arylmethyl)-2-aminomethyl group at 5-position with nanomolar to mid-nanomolar binding affinities measured with the BRET method. Another series included **A26**, which is 3-acetamido-5-anilino pyrazolo-[3,4-*c*]pyridine and its analogues **L12, L15, L21**. This second series had low micromolar to 100 nM binding affinity against A_1R and A_3R. For the determination of the antagonistic activities, functional assays were applied which measured the inhibition of agonist NECA based on cAMP accumulation, against both A_1R and A_3R.

Compounds **A17, L4** displayed nanomolar affinities and **A26, L5, L8, L9** mid-nanomolar affinities to the A_3R (**A17**, pK_d = 7.87 ± 0.18; **L4** pK_d = 7.77 ± 0.16; **A26**, pK_d = 7.05 ± 0.22; **L5**, pK_d = 7.05 ± 0.20; **L8**, pK_d = 6.80 ± 0.24; **L9**, pK_d = 6.89 ± 0.2). At the A_1R, **A17**, displayed low nanomolar affinity and the five compounds **L4, L6-L9, L12** displayed mid-nanomolar to low nanomolar affinities (**A17** pK_d = 8.25 ± 0.15; **L4** pK_d =7.04 ± 0.14; **L6** pK_d = 6.84 ± 0.23; **L7** pK_d =7.29 ± 0.18; **L8**, pK_d = 7.18 ± 0.25; **L9**, pK_d = 6.99 ± 0.16; **L12** pK_d = 6.71 ± 0.14).

Although, the binding areas of ARs are broad, it is very interesting to observe that small changes in ligand's structure resulted in significant changes in affinity/activity and receptor selectivity. For example, the replacement in **A17** of the 5-cyano by the chloro group in **L5** reduced the affinity by ca. 7-fold and the deletion of the cyano group reduced the affinity by ca. 20-fold against A_3R while by 100-fold and by 30-fold to A_1R, respectively.

Some compounds showed high affinities and a diverse range of kinetic profiles. We found A_3R and A_1R antagonists with medium RT and much longer RTs. For compounds acting at the A_3R **A17, L4, L5** had the longer residence time with RT values between ca. 32-50 mins and **L6, L7, L10, A26** the shortest residence with RT values between ca. 5.6-11 mins. For compounds acting at the A_1R **A15, A17, L9, L10** had the longer residence time with RT values between ca. 30-44 mins and **L3, L5, L8, A26, L15** the shortest residence with RT values between ca. 7.5-19 mins. Compounds which displayed high affinity at the A_3R, had RT between ca. 5-50 mins, and at A_1R between ca. 18-40 min (**L4, L6-L8**). The kinetic data showed that compared to not potent congeners the active compounds which displayed high affinity have similar association rate, for example at A_3R K_{on} = 21.3 x10^5 M^{-1} (**A17**) vs K_{on} = 4.8 x10^5 M^{-1} (**L7**) but much lower dissociation rate K_{off} = 0.021 min^{-1} (**A17**) vs 0.105 min^{-1} (**L7**) resulting in lower K_d's. Knowledge of target binding kinetics has been discussed to be very important for developing and selecting new AR antagonists in the early phase of drug discovery. [37,141]

We performed MD simulations for all the ligands **A15, L2-L10, A17** and **A26, L12, L15, L21** against A_1R, A_3R and observed that **A17**, which is low nanomolar at both A_1R and A_3R ligands, is stabilized

inside the binding area by an array of co-operative interactions. Compound **A17** binds to A_1R and interacts with TM5 E170$^{5.28}$, F171$^{5.29}$, E172$^{5.30}$, M180$^{5.38}$, N184$^{5.42}$, TM6 W247$^{6.48}$, L250$^{6.51}$, H251$^{6.52}$, N254$^{6.55}$, TM7 T270$^{7.35}$, Y271$^{7.36}$ in A_1R. [142] In the case of **L9**, having an increased girth compared to **A17** due to the replacement of the cyano with N-(3-pyridinylmethyl)aminomethyl group the interactions with A_1R also include TM2, TM3 residues, eg. V62$^{2.57}$, A66$^{2.61}$, V87$^{3.32}$ but also additional residues at TM7, eg. I274$^{7.39}$, H278$^{7.43}$. Compound **A17** binds to A_3R and interacts with F168$^{5.29}$, V169$^{5.30}$, F182$^{5.43}$, W243$^{6.48}$, L246$^{6.51}$, N250$^{6.55}$, I253$^{6.58}$, L264$^{7.35}$, Y265$^{7.36}$. Similarly, **L9** interacts additionally with E19$^{1.39}$, V65$^{2.57}$, V72$^{2.64}$, L90$^{3.32}$ but also additional residues at TM5, TM7, eg. Q167$^{5.28}$, M177$^{5.38}$, I274$^{7.39}$.

Selection of residues for mutagenesis experiments were guided by MD simulations for the complex of A_1R with the most potent ligand **A17**. Even for the two experimentally resolved AR subtypes the description of the orthosteric binding area and structure-activity relationships of ligands remains a challenging task due to the high similar amino acids sequence but also the broadness and flexibility of the ARs binding area. Using alanine scanning mutagenesis experiments and the BRET method we observed that mutation to alanine of some residues in proximity to the low nanomolar **A17**, eg. residues E172$^{5.30}$, Y271$^{7.36}$ or S267$^{7.32}$, leave unchanged or reduced affinity, respectively. Strikingly, the L250$^{6.51}$ to alanine mutation increased the affinity. However, L$^{6.51}$ is key-to-recognition and highly conserved residue in all four AR subtypes and until now it was known that its mutation to alanine reduced affinity of both agonists and antagonists. This result suggests that inside the orthosteric binding area in a height where L250$^{6.51}$ is positioned a substituent can added to **A17** to increase binding affinity. We also found that residues distant over 4 Å from the ligand can effect allosterically the binding of **A17**. Mutations T91$^{3.36}$A, H251$^{6.52}$A increased the affinity for **A17** as has been reported previously for $A_{2A}R$ - antagonists [127] or A_1R, $A_{2A}R$-NECA [126] complexes.

We compared the results of two binding free energy calculation methods the one based on empirical approximations and the other on statistical mechanics. The MM-GBSA method, using an implicit membrane model and the waters in the binding area, calculated roughly binding free energy changes caused by the addition or deletion of a substituent but can't predict the effect of changing a substituent by another. In contrast, the TI/MD method produced strong spearman rank correlation (p = 0.82 and 0.84) for A_1R and A_3R, respectively, between the calculated and experimental relative binding free energies and can be used for structure-based improvement of **A17**.

Conclusion

We identified from the re-purposing of *in-house* antiproliferative compounds the novel pyrazolo[3,4-c]pyridine scaffold than can lead to ligands of ARs and improved understanding of structure-activity relationships (SAR) of ligands targeting ARs. After testing of pyrazolo[3,4-c]pyridine derivatives against all four AR subtypes we identified binding affinity and antagonistic activity against A_1R and A_3R. We found one series of potent derivatives with phenyl group at 3-position, anilino group at 7-position and cyano group at 5-position and one series with acetamido group at 3-position and anilino group at 5-position. Thus, **A17, L4** displayed nanomolar affinities and **L5, L8, L9** mid-nanomolar affinities to the A_3R. At the A_1R, **A17**, displayed low nanomolar affinity and the five compounds **L4, L6-L9, L12** displayed mid-nanomolar to low nanomolar.

We investigated particularly the molecular recognition of A_1R and A_3R from the analogues of the most potent antagonist **A17**, which has a 3-phenyl, 5-cyano and 7-(3,4,5-trimethoxy)anilino substitution pattern, using a combination of functional assays, binding kinetics, site-directed mutagenesis, MD simulations and accurate binding free energy calculations with the TI/MD method, first applied on a GPCR system including the whole membrane and showing a very good agreement between calculated and experimental relative binding free energies for A_1R and A_3R (p = 0.82 and 0.84, respectively). A novel observation from mutagenesis data for drug design purposes is that when the L250$^{6.51}$A is changed to alanine the binding affinity of **A17** significantly increased at A_1R.

Compound **A17** has a K_d = 5.62 nM and RT = 41.33 min measured using a NanoBRET assay for A_1R and K_d = 13.5 nM and RT = 47.23 min for A_3R. The kinetic data showed that compared to not potent congeners, **A17** has similar association but much lower dissociation rate (eg. at A_1R K_{on} = 139.7 x10^5 M^{-1} and K_{off} = 0.024 min^{-1}). **A17** is a new low nanomolar lead which can afford by means of TI/MD and kinetic experiments ligands with improved affinity and selectivity.

Supporting Information available

Supporting information includes supplementary information for the simulations methods, MD simulations results, and MM-GBSA calculations results. Also supporting information includes five Tables, four Figures. One Table with chemical structures of compounds from our in-house library; one Table with functional activities for **A15, A17** and **A27** against $A_{2A}R$ and $A_{2B}R$; one Table with pIC_{50} of NECA in the presence of DMSO and in the presence of a potential antagonist in A_3R and A_1R Flp-In^{TM} CHO cells; one Table with functional activities for **L2-L10**, and **L12, L15, L21** against $A_{2A}R$ and $A_{2B}R$; one Table with MM-GBSA-calculated ΔG_{eff} and RMSD values of the ligand and protein Ca carbons. One Figure showing the screening for potential antagonists at the A_1R and A_3R, where cAMP accumulation was determined in Flp-In CHO cells stably expressing A_3R co-stimulated with 10 μM forskolin, NECA at the pre-determined IC_{80} concentration (3.16 nM) and 1 μM of compound/DMSO control; one Figure showing the characterisation of **A15/A17** and **A26** analogues' selectivity, at the $A_{2A}R$ and $A_{2B}R$; one Figure showing frames, RMSD plots and frequency interaction plots for A_1R, A_3R in complex with antagonists not shown in the manuscript; one Figure showing as bars ΔG_{eff} values from MM-GBSA calculations and experimental binding affinities calculated using the pK_d values for A_1R and A_3R.

Acknowledgements

Author Information

Address for correspondence. Dr Antonios Kolocouris, Laboratoty of Medicinal Chemistry, Section of Pharmaceutical Chemistry, Department of Pharmacy, National and Kapodistrian University of Athens, Panepistimiopolis Zografou, Athens, 15771. Tel: 210-727-4834, Email: ankol@pharm.uoa.gr.

Dr Graham Ladds, Department of Pharmacology, University of Cambridge, Tennis Court Road, Cambridge, CB2 1PD Tel; +44 (0) 1223 334020. Email: grl30@cam.ac.uk.

KB present address: Socei Heptares, Steinmetz Building, Granta Park, Cambridge CB21 6DG, UK

Abbreviations

ARs, adenosine receptors; CG, conjugate-gradient; CNS, central nervous system; cAMP, 3',5'-cyclic adenosine monophosphate; COPD, chronic obstructive pulmonary disease; CPT, 8-cyclopentyl-1,3-dimethylxanthine; DMSO, dimethyl sulfoxide; GAFF, Generalized Amber Force Field; Extracellular loop, EL2; FEP, Free Energy Perturbation; GB, Generalized-Born; GUI, graphical user interface; GPCRs, G-protein coupled receptors; HF, Hartree-Fock; IB-MECA, N6-(3-iodobenzyl)-adenosine-5'-N-methylcarboxamide; IL, intracellular loop; LJ-1888, ((2R,3R,4S)-2-[2-chloro-6-(3-iodobenzylamino)-9H-purine-9-yl]tetrahydrothiophene-3,4-diol); m.a.e., mean assigned error, MM-GBSA, molecular mechanics-Generalized Born Surface Area; MARK, mitogen-activated protein kinase; MD, molecular dynamics; MRS1220, N-[9-chloro-2-(2-furanyl)-1,2,4-triazolo[1,5-c]quinazolin-5-yl]benzeneacetamide; NanoBRET, Nano Bioluminescence resonance energy transfer; NECA, 5'-N-ethylcarboxamidoadenosine; NPT, constant pressure, temperature and number of atoms; NVT, constant volume, temperature and number of atoms, OPM, Orientations of Proteins in Membranes; PDB, Protein data bank; PME, particle mesh Ewald method; POPE, 1-palmitoyl-2-oleoyl-*sn*-glycero-3-phosphoethanolamine; residence time, RT; RESPA, Reversible multiple time scale molecular dynamics; RMS, root-mean-square; RMSD, root-mean-square deviation; SAR, structure-activity relationship; SASA, solvent accessible surface area, SID, Simulation Interaction Diagram; TM, Transmembrane; TI/MD, thermodynamics

integration coupled with MD simulations; Tc, TanimotoCombo coefficient; XAC, xanthine amine congener

References

(1)   Fredholm, B. B.; IJzerman, A. P.; Jacobson, K. A.; Linden, J.; Müller, C. E. International Union of Basic and Clinical Pharmacology. LXXXI. Nomenclature and Classification of Adenosine Receptors—an Update. *Pharmacol. Rev.* **2011**, pr--110.

(2)   Lebon, G.; Warne, T.; Edwards, P. C.; Bennett, K.; Langmead, C. J.; Leslie, A. G. W.; Tate, C. G. Agonist-Bound Adenosine A2A Receptor Structures Reveal Common Features of GPCR Activation. *Nature* **2011**, *474*, 521–525.

(3)   Carpenter, B.; Nehmé, R.; Warne, T.; Leslie, A. G. W.; Tate, C. G. Structure of the Adenosine A2A Receptor Bound to an Engineered G Protein. *Nature* **2016**, *536*, 104–107.

(4)   García-Nafría, J.; Lee, Y.; Bai, X.; Carpenter, B.; Tate, C. G. Cryo-EM Structure of the Adenosine A2Areceptor Coupled to an Engineered Heterotrimeric G Protein. *Elife* **2018**, *7:e35946*, 1–19.

(5)   Jaakola, V.-P.; Griffith, M. T.; Hanson, M. A.; Cherezov, V.; Chien, E. Y. T.; Lane, J. R.; IJzerman, A. P.; Stevens, R. C. The 2.6 Angstrom Crystal Structure of a Human A2A Adenosine Receptor Bound to an Antagonist. *Science (80-.).* **2008**, *322*, 1211–1217.

(6)   Doré, A. S.; Robertson, N.; Errey, J. C.; Ng, I.; Hollenstein, K.; Tehan, B.; Hurrell, E.; Bennett, K.; Congreve, M.; Magnani, F.; Tate, C. G.; Weir, M.; Marshall, F. H. Structure of the Adenosine A(2A) Receptor in Complex with ZM241385 and the Xanthines XAC and Caffeine. *Structure* **2011**, *19*, 1283–1293.

(7)   Liu, W.; Chun, E.; Thompson, A. A.; Chubukov, P.; Xu, F.; Katritch, V.; Han, G. W.; Roth, C. B.; Heitman, L. H.; IJzerman, A. P.; Cherezov, V.; Stevens, R. C. Structural Basis for Allosteric Regulation of GPCRs by Sodium Ions. *Science (80-.).* **2012**, *337*, 232–236.

(8)   Sun, B.; Bachhawat, P.; Chu, M. L.-H.; Wood, M.; Ceska, T.; Sands, Z. A.; Mercier, J.; Lebon, F.; Kobilka, T. S.; Kobilka, B. K. Crystal Structure of the Adenosine A 2A Receptor Bound to an Antagonist Reveals a Potential Allosteric Pocket. *Proc. Natl. Acad. Sci.* **2017**, *114*, 2066–2071.

(9)   Amelia, T.; van Veldhoven, J. P. D.; Falsini, M.; Liu, R.; Heitman, L. H.; van Westen, G. J. P.; Segala, E.; Verdon, G.; Cheng, R. K. Y.; Cooke, R. M.; van der Es, D.; IJzerman, A. P. Crystal Structure and Subsequent Ligand Design of a Nonriboside Partial Agonist Bound to the Adenosine A 2A Receptor. *J. Med. Chem.* **2021**, *64*, 3827–3842.

(10)   Glukhova, A.; Thal, D. M.; Nguyen, A. T.; Vecchio, E. A.; Jörg, M.; Scammells, P. J.; May, L. T.; Sexton, P. M.; Christopoulos, A. Structure of the Adenosine A1 Receptor Reveals the Basis for Subtype Selectivity. *Cell* **2017**, *168*, 867-877.e13.

(11)   Cheng, R. K. Y.; Segala, E.; Robertson, N.; Deflorian, F.; Doré, A. S.; Errey, J. C.; Fiez-Vandal, C.; Marshall, F. H.; Cooke, R. M. Structures of Human A1 and A2A Adenosine Receptors with Xanthines Reveal Determinants of Selectivity. *Structure* **2017**, *25*, 1275–1285.

(12)   Katritch, V.; Jaakola, V. P.; Lane, J. R.; Lin, J.; Ijzerman, A. P.; Yeager, M.; Kufareva, I.; Stevens, R. C.; Abagyan, R. Structure-Based Discovery of Novel Chemotypes for Adenosine A2Areceptor Antagonists. *J. Med. Chem.* **2010**, *53*, 1799–1809.

(13)   Carlsson, J.; Yoo, L.; Gao, Z. G.; Irwin, J. J.; Shoichet, B. K.; Jacobson, K. A. Structure-Based Discovery of A2Aadenosine Receptor Ligands. *J. Med. Chem.* **2010**, *53*, 3748–3755.

(14)   Lenselink, E. B.; Beuming, T.; van Veen, C.; Massink, A.; Sherman, W.; van Vlijmen, H. W. T.; IJzerman, A. P. In Search of Novel Ligands Using a Structure-Based Approach: A Case Study on the Adenosine A2A Receptor. *J. Comput. Aided. Mol. Des.* **2016**, *30*, 863–874.

(15)   Cescon, E.; Bolcato, G.; Federico, S.; Bissaro, M.; Valentini, A.; Ferlin, M. G.; Spalluto, G.; Sturlese, M.; Moro, S. Scaffold Repurposing of In-House Chemical Library toward the Identification of New Casein Kinase 1 Inhibitors. *ACS Med. Chem. Lett.* **2020**, *11*, 1168–1174.

(16)   Langmead, C. J.; Andrews, S. P.; Congreve, M.; Errey, J. C.; Hurrell, E.; Marshall, F. H.; Mason, J. S.; Richardson, C. M.; Robertson, N.; Zhukov, A.; Weir, M. Identification of Novel Adenosine A2A Receptor Antagonists by Virtual Screening. *J. Med. Chem.* **2012**, *55*, 1904–1909.

(17)   Jazayeri, A.; Andrews, S. P.; Marshall, F. H. Structurally Enabled Discovery of Adenosine A2A Receptor Antagonists. *Chem. Rev.* **2017**, *117*, 21–37.

(18)   Tian, S.; Wang, X.; Li, L.; Zhang, X.; Li, Y.; Zhu, F.; Hou, T.; Zhen, X. Discovery of Novel and Selective Adenosine A2A Receptor Antagonists for Treating Parkinson's Disease through Comparative Structure-Based Virtual Screening. *J. Chem. Inf. Model.* **2017**, *57*, 1474–1487.

(19)   Lagarias, P.; Vrontaki, E.; Lambrinidis, G.; Stamatis, D.; Convertino, M.; Ortore, G.;

Mavromoustakos, T.; Klotz, K.-N.; Kolocouris, A. Discovery of Novel Adenosine Receptor Antagonists through a Combined Structure- and Ligand-Based Approach Followed by Molecular Dynamics Investigation of Ligand Binding Mode. *J. Chem. Inf. Model.* **2018**, *58*, 794–815.

(20) Barkan, K.; Lagarias, P.; Stampelou, M.; Stamatis, D.; Hoare, S.; Safitri, D.; Klotz, K.-N.; Vrontaki, E.; Kolocouris, A.; Ladds, G. Pharmacological Characterisation of Novel Adenosine A3 Receptor Antagonists. *Sci. Rep.* **2020**, *10*, 20781.

(21) Stamatis, D.; Lagarias, P.; Barkan, K.; Vrontaki, E.; Ladds, G.; Kolocouris, A. Structural Characterization of Agonist Binding to an A 3 Adenosine Receptor through Biomolecular Simulations and Mutagenesis Experiments . *J. Med. Chem.* **2019**, *62*, 8831–8846.

(22) Lagarias, P.; Barkan, K.; Tzortzini, E.; Stampelou, M.; Vrontaki, E.; Ladds, G.; Kolocouris, A. Insights to the Binding of a Selective Adenosine A3 Receptor Antagonist Using Molecular Dynamic Simulations, MM-PBSA and MM-GBSA Free Energy Calculations, and Mutagenesis. *J. Chem. Inf. Model.* **2019**, *59*, 5183–5197.

(23) Schenone, S.; Brullo, C.; Musumeci, F.; Bruno, O.; Botta, M. A1 Receptors Ligands: Past, Present and Future Trends. *Curr. Top. Med. Chem.* **2010**, *10*, 878–901.

(24) Modlinger, P. S.; Welch, W. J. Adenosine A1 Receptor Antagonists and the Kidney. *Curr. Opin. Nephrol. Hypertens.* **2003**, *12*, 497–502.

(25) Shah, R. H.; Frishman, W. H. Adenosine1 Receptor Antagonism: A New Therapeutic Approach for the Treatment of Decompensated Heart Failure. *Cardiol. Rev.* **2009**, *17*, 125–131.

(26) Wilson, C. N.; Nadeem, A.; Spina, D.; Brown, R.; Page, C. P.; Mustafa, S. J. Adenosine Receptors and Asthma. In *Handbook of Experimental Pharmacology*; 2009; pp. 329–362.

(27) Maemoto, T.; Tada, M.; Mihara, T.; Ueyama, N.; Matsuoka, H.; Harada, K.; Yamaji, T.; Shirakawa, K.; Kuroda, S.; Akahane, A.; Iwashita, A.; Matsuoka, N.; Mutoh, S. Pharmacological Characterization of FR194921, a New Potent, Selective, and Orally Active Antagonist for Central Adenosine A1 Receptors. *J. Pharmacol. Sci.* **2004**, *96*, 42–52.

(28) Trevitt, J.; Vallance, C.; Harris, A.; Goode, T. Adenosine Antagonists Reverse the Cataleptic Effects of Haloperidol: Implications for the Treatment of Parkinson's Disease. *Pharmacol. Biochem. Behav.* **2009**, *92*, 521–527.

(29) Borea, P. A.; Varani, K.; Vincenzi, F.; Baraldi, P. G.; Tabrizi, M. A.; Merighi, S.; Gessi, S.; Cacciari, B.; Romagnoli, R.; Merighi, S.; Varani, K.; Borea, P. A.; Spalluto, G. The A3 Adenosine Receptor: History and Perspectives. *Pharmacol. Rev.* **2015**, *67*, 74–102.

(30) Schulte, G.; Fredholm, B. B. Signaling Pathway from the Human Adenosine A 3 Receptor Expressed in Chinese Hamster Ovary Cells to the Extracellular Signal-Regulated Kinase 1/2. *Mol. Pharmacol.* **2002**, *62*, 1137–1146.

(31) Lee, J.; Hwang, I.; Lee, J. H.; Lee, H. W.; Jeong, L.-S.; Ha, H. The Selective A3AR Antagonist LJ-1888 Ameliorates UUO-Induced Tubulointerstitial Fibrosis. *Am. J. Pathol.* **2013**, *183*, 1488–1497.

(32) Rabadi, M. M.; Lee, H. T. Adenosine Receptors and Renal Ischaemia Reperfusion Injury. *Acta Physiol. (Oxf).* **2015**, *213*, 222–231.

(33) González-Fernández, E.; Sánchez-Gómez, M. V.; Pérez-Samartín, A.; Arellano, R. O.; Matute, C. A 3 Adenosine Receptors Mediate Oligodendrocyte Death and Ischemic Damage to Optic Nerve. *Glia* **2014**, *62*, 199–216.

(34) Baraldi, P. G.; Preti, D.; Borea, P. A.; Varani, K. Medicinal Chemistry of A 3 Adenosine Receptor Modulators: Pharmacological Activities and Therapeutic Implications. *J. Med. Chem.* **2012**, *55*, 5676–5703.

(35) Guo, D.; Heitman, L. H.; IJzerman, A. P. Kinetic Aspects of the Interaction between Ligand and G Protein-Coupled Receptor: The Case of the Adenosine Receptors. *Chem. Rev.* **2017**, *117*, 38–66.

(36) Sykes, D. A.; Stoddart, L. A.; Kilpatrick, L. E.; Hill, S. J. Binding Kinetics of Ligands Acting at GPCRs. *Mol. Cell. Endocrinol.* **2019**, *485*, 9–19.

(37) Xia, L.; Burger, W. A. C.; van Veldhoven, J. P. D.; Kuiper, B. J.; van Duijl, T. T.; Lenselink, E. B.; Paasman, E.; Heitman, L. H.; IJzerman, A. P. Structure–Affinity Relationships and Structure–Kinetics Relationships of Pyrido[2,1- f]Purine-2,4-Dione Derivatives as Human Adenosine A 3 Receptor Antagonists. *J. Med. Chem.* **2017**, *60*, 7555–7568.

(38) Bouzo-Lorenzo, M.; Stoddart, L. A.; Xia, L.; IJzerman, A. P.; Heitman, L. H.; Briddon, S. J.; Hill, S. J. A Live Cell NanoBRET Binding Assay Allows the Study of Ligand-Binding Kinetics to the Adenosine A3 Receptor. *Purinergic Signal.* **2019**, *15*, 139–153.

(39) Guo, D.; van Dorp, E. J. H.; Mulder-Krieger, T.; van Veldhoven, J. P. D.; Brussee, J.; IJzerman, A. P.; Heitman, L. H. Dual-Point Competition Association Assay. *J. Biomol. Screen.* **2013**, *18*, 309–320.

(40) Guo, D.; Venhorst, S. N.; Massink, A.; van Veldhoven, J. P. D.; Vauquelin, G.; IJzerman, A. P.; Heitman, L. H. Molecular Mechanism of Allosteric Modulation at GPCRs: Insight from

a Binding Kinetics Study at the Human A 1 Adenosine Receptor. *Br. J. Pharmacol.* **2014**, *171*, 5295–5312.

(41) Louvel, J.; Guo, D.; Soethoudt, M.; Mocking, T. A. M.; Lenselink, E. B.; Mulder-Krieger, T.; Heitman, L. H.; IJzerman, A. P. Structure-Kinetics Relationships of Capadenoson Derivatives as Adenosine A 1 Receptor Agonists. *Eur. J. Med. Chem.* **2015**, *101*, 681–691.

(42) Müller, C. E.; Diekmann, M.; Thorand, M.; Ozola, V. [3H]8-Ethyl-4-Methyl-2-Phenyl-(8R)-4,5,7,8-Tetrahydro-1H-Imidazo[2,1-i]-Purin-5-One ([3H]PSB-11), a Novel High-Affinity Antagonist Radioligand for Human A3 Adenosine Receptors. *Bioorg. Med. Chem. Lett.* **2002**, *12*, 501–503.

(43) Varani, K.; Merighi, S.; Gessi, S.; Klotz, K. N.; Leung, E.; Baraldi, P. G.; Cacciari, B.; Romagnoli, R.; Spalluto, G.; Borea, P. A. [(3)H]MRE 3008F20: A Novel Antagonist Radioligand for the Pharmacological and Biochemical Characterization of Human A(3) Adenosine Receptors. *Mol. Pharmacol.* **2000**, *57*, 968–975.

(44) Giannouli, V.; Lougiakis, N.; Kostakis, I. K.; Pouli, N.; Marakos, P.; Skaltsounis, A.-L.; Nam, S.; Jove, R.; Horne, D.; Tenta, R.; Pratsinis, H.; Kletsas, D. The Discovery of New Cytotoxic Pyrazolopyridine Derivatives. *Bioorg. Med. Chem. Lett.* **2016**, *26*, 5229–5233.

(45) Sklepari, M.; Lougiakis, N.; Papastathopoulos, A.; Pouli, N.; Marakos, P.; Myrianthopoulos, V.; Robert, T.; Bach, S.; Mikros, E.; Ruchaud, S. Synthesis, Docking Study and Kinase Inhibitory Activity of a Number of New Substituted Pyrazolo[3,4-c]Pyridines. *Chem. Pharm. Bull. (Tokyo).* **2017**, *65*, 66–81.

(46) Argyros, O.; Lougiakis, N.; Kouvari, E.; Papafotika, A.; Raptopoulou, C. P.; Psycharis, V.; Christoforidis, S.; Pouli, N.; Marakos, P.; Tamvakopoulos, C. Design and Synthesis of Novel 7-Aminosubstituted Pyrido[2,3-b]Pyrazines Exhibiting Anti-Breast Cancer Activity. *Eur. J. Med. Chem.* **2017**, *126*, 954–968.

(47) Papastathopoulos, A.; Lougiakis, N.; Kostakis, I. K.; Marakos, P.; Pouli, N.; Pratsinis, H.; Kletsas, D. New Bioactive 5-Arylcarboximidamidopyrazolo[3,4-c]Pyridines: Synthesis, Cytotoxic Activity, Mechanistic Investigation and Structure-Activity Relationships. *Eur. J. Med. Chem.* **2021**, *218*, 113387.

(48) Michailidou, M.; Giannouli, V.; Kotsikoris, V.; Papadodima, O.; Kontogianni, G.; Kostakis, I. K.; Lougiakis, N.; Chatziioannou, A.; Kolisis, F. N.; Marakos, P.; Pouli, N.; Loutrari, H. Novel Pyrazolopyridine Derivatives as Potential Angiogenesis Inhibitors: Synthesis, Biological Evaluation and Transcriptome-Based Mechanistic Analysis. *Eur. J. Med. Chem.* **2016**, *121*, 143–157.

(49) Evangelou, K.; Lougiakis, N.; Rizou, S. V.; Kotsinas, A.; Kletsas, D.; Muñoz-Espín, D.; Kastrinakis, N. G.; Pouli, N.; Marakos, P.; Townsend, P.; Serrano, M.; Bartek, J.; Gorgoulis, V. G. Robust, Universal Biomarker Assay to Detect Senescent Cells in Biological Specimens. *Aging Cell* **2017**, *16*, 192–197.

(50) Gerasi, M.; Frakolaki, E.; Papadakis, G.; Chalari, A.; Lougiakis, N.; Marakos, P.; Pouli, N.; Vassilaki, N. Design, Synthesis and Anti-HBV Activity Evaluation of New Substituted Imidazo[4,5-b]Pyridines. *Bioorg. Chem.* **2020**, *98*, 103580.

(51) Lougiakis, N.; Marakos, P.; Pouli, N.; Fragopoulou, E.; Tenta, R. Synthesis of New Nebularine Analogues and Their Inhibitory Activity against Adenosine Deaminase. *Chem. Pharm. Bull.* **2015**, *63*, 134–142.

(52) Lougiakis, N.; Frakolaki, E.; Karmou, P.; Pouli, N.; Marakos, P.; Madan, V.; Bartenschlager, R.; Vassilaki, N. Novel Nucleoside Analogues Targeting HCV Replication through an NS5A-Dependent Inhibition Mechanism. *Chem. Biol. Drug Des.* **2017**, *90*, 352–367.

(53) Papadakis, G.; Gerasi, M.; Snoeck, R.; Marakos, P.; Andrei, G.; Lougiakis, N.; Pouli, N. Synthesis of New Imidazopyridine Nucleoside Derivatives Designed as Maribavir Analogues. *Molecules* **2020**, *25*, 4531.

(54) Massova, I.; Kollman, P. A. *Combined Molecular Mechanical and Continuum Solvent Approach (MM- PBSA/GBSA) to Predict Ligand Binding*; 2000; Vol. 18, pp. 113–135.

(55) Greene, D.; Qi, R.; Nguyen, R.; Qiu, T.; Luo, R. Heterogeneous Dielectric Implicit Membrane Model for the Calculation of MMPBSA Binding Free Energies. *J. Chem. Inf. Model.* **2019**, *59*, 3041–3056.

(56) Aldeghi, M.; Bodkin, M. J.; Knapp, S.; Biggin, P. C. Statistical Analysis on the Performance of Molecular Mechanics Poisson–Boltzmann Surface Area versus Absolute Binding Free Energy Calculations: Bromodomains as a Case Study. *J. Chem. Inf. Model.* **2017**, *57*, 2203–2221.

(57) Lenselink, E. B.; Louvel, J.; Forti, A. F.; van Veldhoven, J. P. D.; de Vries, H.; Mulder-Krieger, T.; McRobb, F. M.; Negri, A.; Goose, J.; Abel, R.; van Vlijmen, H. W. T.; Wang, L.; Harder, E.; Sherman, W.; IJzerman, A. P.; Beuming, T. Predicting Binding Affinities for GPCR Ligands Using Free-Energy Perturbation. *ACS Omega* **2016**, *1*, 293–304.

(58) Weston, C.; Poyner, D.; Patel, V.; Dowell, S.; Ladds, G. Investigating G Protein Signalling Bias at the Glucagon-like Peptide-1 Receptor in Yeast. *Br. J. Pharmacol.* **2014**, *171*, 3651–

3665.

(59) Knight, A.; Hemmings, J. L.; Winfield, I.; Leuenberger, M.; Frattini, E.; Frenguelli, B. G.; Dowell, S. J.; Lochner, M.; Ladds, G. Discovery of Novel Adenosine Receptor Agonists That Exhibit Subtype Selectivity. *J. Med. Chem.* **2016**, *59*, 947–964.

(60) Deganutti, G.; Barkan, K.; Ladds, G.; Reynolds, C. A. Multisite Model of Allosterism for the Adenosine A1 Receptor. *J. Chem. Inf. Model.* **2021**, *61*, 2001–2015.

(61) Zhang, G.; Liu, Y.; Ruoho, A. E.; Hurley, J. H. Structure of the Adenylyl Cyclase Catalytic Core. *Nature* **1997**, *386*, 247–253.

(62) Motulsky, H. J.; Mahan, L. C. The Kinetics of Competitive Radioligand Binding Predicted by the Law of Mass Action. *Mol. Pharmacol.* **1984**, *25*, 1–9.

(63) Tallarida, R. J.; Murray, R. B. *Manual of Pharmacologic Calculations*; Springer New York: New York, NY, 1986.

(64) Stoddart, L. A.; Johnstone, E. K. M.; Wheal, A. J.; Goulding, J.; Robers, M. B.; Machleidt, T.; Wood, K. V.; Hill, S. J.; Pfleger, K. D. G. Application of BRET to Monitor Ligand Binding to GPCRs. *Nat. Methods* **2015**, *12*, 661–663.

(65) Curtis, M. J.; Alexander, S.; Cirino, G.; Docherty, J. R.; George, C. H.; Giembycz, M. A.; Hoyer, D.; Insel, P. A.; Izzo, A. A.; Ji, Y.; MacEwan, D. J.; Sobey, C. G.; Stanford, S. C.; Teixeira, M. M.; Wonnacott, S.; Ahluwalia, A. Experimental Design and Analysis and Their Reporting II: Updated and Simplified Guidance for Authors and Peer Reviewers. *British Journal of Pharmacology*, 2018, 175(7):987-993.

(66) Duan, J.; Dixon, S. L.; Lowrie, J. F.; Sherman, W. Analysis and Comparison of 2D Fingerprints: Insights into Database Screening Performance Using Eight Fingerprint Methods. *J. Mol. Graph. Model.* **2010**, *29*, 157–170.

(67) Hawkins, P. C. D.; Skillman, A. G.; Nicholls, A. Comparison of Shape-Matching and Docking as Virtual Screening Tools. *J. Med. Chem.* **2007**, *50*, 74–82.

(68) Jones, G.; Willett, P.; Glen, R. C.; Leach, A. R.; Taylor, R. Development and Validation of a Genetic Algorithm for Flexible Docking. *J. Mol. Biol.* **1997**, *267*, 727–748.

(69) Eldridge, M. D.; Murray, C. W.; Auton, T. R.; Paolini, G. V; Mee, R. P. Empirical Scoring Functions: I. The Development of a Fast Empirical Scoring Function to Estimate the Binding Affinity of Ligands in Receptor Complexes. *J. Comput. Aided. Mol. Des.* **1997**, *11*, 425–445.

(70) Lomize, M. A.; Pogozheva, I. D.; Joo, H.; Mosberg, H. I.; Lomize, A. L. OPM Database and PPM Web Server: Resources for Positioning of Proteins in Membranes. *Nucleic Acids Res.* **2012**, *40*, D370–D376.

(71) Jorgensen, W. L.; Chandrasekhar, J.; Madura, J. D.; Impey, R. W.; Klein, M. L. Comparison of Simple Potential Functions for Simulating Liquid Water. *J. Chem. Phys.* **1983**, *79*, 926–935.

(72) Wang, J.; Cieplak, P.; Kollman, P. A. How Well Does a Restrained Electrostatic Potential (RESP) Model Perform in Calculating Conformational Energies of Organic and Biological Molecules? *J. Comput. Chem.* **2000**, *21*, 1049–1074.

(73) Hornak, V.; Abel, R.; Okur, A.; Strockbine, B.; Roitberg, A.; Simmerling, C. Comparison of Multiple Amber Force Fields and Development of Improved Protein Backbone Parameters. *Proteins Struct. Funct. Bioinforma.* **2006**, *65*, 712–725.

(74) Wang, J.; Wolf, R. M.; Caldwell, J. W.; Kollman, P. A.; Case, D. A. Development and Testing of a General Amber Force Field. *J. Comput. Chem.* **2004**, *25*, 1157–1174.

(75) Bayly, C. I.; Cieplak, P.; Cornell, W. D.; Kollman, P. A. A Well-Behaved Electrostatic Potential Based Method Using Charge Restraints for Deriving Atomic Charges: The RESP Model. *J. Phys. Chem.* **1993**, *97*, 10269–10280.

(76) M. J. Frisch, G. W. Trucks, H. B. Schlegel, G. E. Scuseria, M. A. Robb, J. R. Cheeseman, J. A. Montgomery, Jr., T. Vreven, K. N. Kudin, J. C. Burant, J. M. Millam, S. S. Iyengar, J. Tomasi, V. Barone, B. Mennucci, M. Cossi, G. Scalmani, N. Rega, G. A. Pet, 2003. Gaussian 03.

(77) DAVIDSON, E. R.; FELLER, D. Basis Set Selection for Molecular Calculations. *Chem. Rev.* **1986**, *86*, 681–696.

(78) D.A. Case; I.Y. Ben-Shalom; S.R. Brozell; D.S. Cerutti; T.E. Cheatham; III, V. W. D. C.; T.A. Darden; R.E. Duke; D. Ghoreishi; M.K. Gilson; H. Gohlke; A.W. Goetz; D. Greene; R Harris; N. Homeyer; S. Izadi; A. Kovalenko; T. Kurtzman; T.S. Lee; S. LeGrand; P. Li; C. Lin; J. Liu; T. Luchko; R. Luo; D.J. Mermelstein; K.M. Merz; Y. Miao; G. Monard; C. Nguyen; H. Nguyen; I. Omelyan; A. Onufriev; F. Pan; R. Qi; D.R. Roe; A. Roitberg; C. Sagui; S. Schott-Verdugo; J. Shen; C.L. Simmerling; J. Smith; R. Salomon-Ferrer; J. Swails; R.C. Walker; J. Wang; H. Wei; R.M. Wolf; X. Wu; L. Xiao; D.M. York; P.A. Kollman. *AMBER 2018, University of California*; 2018.

(79) Bowers, K. J.; Sacerdoti, F. D.; Salmon, J. K.; Shan, Y.; Shaw, D. E.; Chow, E.; Xu, H.; Dror, R. O.; Eastwood, M. P.; Gregersen, B. A.; Klepeis, J. L.; Kolossvary, I.; Moraes, M. A. Molecular Dynamics---Scalable Algorithms for Molecular Dynamics Simulations on

Commodity Clusters. In *Proceedings of the 2006 ACM/IEEE conference on Supercomputing - SC '06*; ACM Press: New York, New York, USA, New York, USA, 2006; p. 84.

(80) Genheden, S.; Ryde, U. The MM/PBSA and MM/GBSA Methods to Estimate Ligand-Binding Affinities. *Expert Opin. Drug Discov.* **2015**, *10*, 449–461.

(81) Homeyer, N.; Gohlke, H. Free Energy Calculations by the Molecular Mechanics Poisson-Boltzmann Surface Area Method. *Mol. Inform.* **2012**, *31*, 114–122.

(82) Kaminski, G. A.; Friesner, R. A.; Tirado-Rives, J.; Jorgensen, W. L. Evaluation and Reparametrization of the OPLS-AA Force Field for Proteins via Comparison with Accurate Quantum Chemical Calculations on Peptides †. *J. Phys. Chem. B* **2001**, *105*, 6474–6487.

(83) Shivakumar, D.; Williams, J.; Wu, Y. J.; Damm, W.; Shelley, J.; Sherman, W. Prediction of Absolute Solvation Free Energies Using Molecular Dynamics Free Energy Perturbation and the OPLS Force Field. *J. Chem. Theory Comput.* **2010**, *6*, 1509–1519.

(84) Michaud-Agrawal, N.; Denning, E. J.; Woolf, T. B.; Beckstein, O. MDAnalysis: A Toolkit for the Analysis of Molecular Dynamics Simulations. *J. Comput. Chem.* **2011**, *32*, 2319–2327.

(85) Maffucci, I.; Contini, A. Explicit Ligand Hydration Shells Improve the Correlation between MM-PB/GBSA Binding Energies and Experimental Activities. *J. Chem. Theory Comput.* **2013**, *9*, 2706–2717.

(86) Tanizaki, S.; Feig, M. A Generalized Born Formalism for Heterogeneous Dielectric Environments: Application to the Implicit Modeling of Biological Membranes. *J. Chem. Phys.* **2005**, *122*, 124706.

(87) Kirkwood, J. G. Statistical Mechanics of Fluid Mixtures. *J. Chem. Phys.* **1935**.

(88) Genheden, S.; Nilsson, I.; Ryde, U. Binding Affinities of Factor Xa Inhibitors Estimated by Thermodynamic Integration and MM/GBSA. *J. Chem. Inf. Model.* **2011**, *51*, 947–958.

(89) He, X.; Liu, S.; Lee, T.-S.; Ji, B.; Man, V. H.; York, D. M.; Wang, J. Fast, Accurate, and Reliable Protocols for Routine Calculations of Protein–Ligand Binding Affinities in Drug Design Projects Using AMBER GPU-TI with Ff14SB/GAFF. *ACS Omega* **2020**, *5*, 4611–4619.

(90) Song, L. F.; Lee, T.-S.; Zhu, C.; York, D. M.; Merz, K. M. Using AMBER18 for Relative Free Energy Calculations. *J. Chem. Inf. Model.* **2019**, *59*, 3128–3135.

(91) Jo, S.; Kim, T.; Iyer, V. G.; Im, W. CHARMM-GUI: A Web-Based Graphical User Interface for CHARMM. *J. Comput. Chem.* **2008**, *29*, 1859–1865.

(92) D.A. Case, I.Y. Ben-Shalom, S.R. Brozell, D.S. Cerutti, T.E. Cheatham, III, V.W.D. Cruzeiro, T. A. D.; R.E. Duke, D. Ghoreishi, M.K. Gilson, H. Gohlke, A.W. Goetz, D. Greene, R Harris, N. Homeyer, Y. H.; S. Izadi, A. Kovalenko, T. Kurtzman, T.S. Lee, S. LeGrand, P. Li, C. Lin, J. Liu, T. Luchko, R. Luo, D. J.; Mermelstein, K.M. Merz, Y. Miao, G. Monard, C. Nguyen, H. Nguyen, I. Omelyan, A. Onufriev, F. Pan, R.; Qi, D.R. Roe, A. Roitberg, C. Sagui, S. Schott-Verdugo, J. Shen, C.L. Simmerling, J. Smith, R. SalomonFerrer, J. Swails, R.C. Walker, J. Wang, H. Wei, R.M. Wolf, X. Wu, L. Xiao, D. M. Y. and P. A. K. AMBER18, 2018.

(93) Maier, J. A.; Martinez, C.; Kasavajhala, K.; Wickstrom, L.; Hauser, K. E.; Simmerling, C. Ff14SB: Improving the Accuracy of Protein Side Chain and Backbone Parameters from Ff99SB. *J. Chem. Theory Comput.* **2015**, *11*, 3696–3713.

(94) Wang, J.; Wang, W.; Kollman, P. A.; Case, D. A. Automatic Atom Type and Bond Type Perception in Molecular Mechanical Calculations. *J. Mol. Graph. Model.* **2006**, *25*, 247–260.

(95) Ryckaert, J.-P.; Ciccotti, G.; Berendsen, H. J. . Numerical Integration of the Cartesian Equations of Motion of a System with Constraints: Molecular Dynamics of n-Alkanes. *J. Comput. Phys.* **1977**, *23*, 327–341.

(96) Lee, T.-S.; Hu, Y.; Sherborne, B.; Guo, Z.; York, D. M. Toward Fast and Accurate Binding Affinity Prediction with PmemdGTI: An Efficient Implementation of GPU-Accelerated Thermodynamic Integration. *J. Chem. Theory Comput.* **2017**, *13*, 3077–3084.

(97) Feller, S. E.; Zhang, Y.; Pastor, R. W.; Brooks, B. R. Constant Pressure Molecular Dynamics Simulation: The Langevin Piston Method. *J. Chem. Phys.* **1995**, *103*, 4613.

(98) Lzaguirre, J. A.; Catarello, D. P.; Wozniak, J. M.; Skeel, R. D. Langevin Stabilization of Molecular Dynamics. *J. Chem. Phys.* **2001**, *114*, 2090–2098.

(99) Salomon-Ferrer, R.; Case, D. A.; Walker, R. C. An Overview of the Amber Biomolecular Simulation Package. *Wiley Interdiscip. Rev. Comput. Mol. Sci.* **2013**, *3*, 198–210.

(100) Koynova, R.; Caffrey, M. Phases and Phase Transitions of the Phosphatidylcholines. *Biochim. Biophys. Acta - Rev. Biomembr.* **1998**, *1376*, 91–145.

(101) Berendsen, H. J. C.; Postma, J. P. M.; Van Gunsteren, W. F.; Dinola, A.; Haak, J. R. Molecular Dynamics with Coupling to an External Bath. *J. Chem. Phys.* **1984**, *81*, 3684–3690.

(102) Procacci, P. Multiple Bennett Acceptance Ratio Made Easy for Replica Exchange Simulations. *J. Chem. Phys.* **2013**, *139*, 124105.

(103) Shirts, M. R.; Pande, V. S. Comparison of Efficiency and Bias of Free Energies Computed

by Exponential Averaging, the Bennett Acceptance Ratio, and Thermodynamic Integration. *J. Chem. Phys.* **2005**, *122*, 144107.

(104) Darden, T.; York, D.; Pedersen, L. Particle Mesh Ewald: An Nlog(N) Method for Ewald Sums in Large Systems. *J. Chem. Phys.* **1993**, *98*, 10089–10092.

(105) Essmann, U.; Perera, L.; Berkowitz, M. L.; Darden, T.; Lee, H.; Pedersen, L. G. A Smooth Particle Mesh Ewald Method. *J. Chem. Phys.* **1995**, *103*, 8577–8593.

(106) Steinbrecher, T.; Joung, I.; Case, D. A. Soft-Core Potentials in Thermodynamic Integration: Comparing One- and Two-Step Transformations. *J. Comput. Chem.* **2011**, *32*, 3253–3263.

(107) Su, P.-C.; Johnson, M. E. Evaluating Thermodynamic Integration Performance of the New Amber Molecular Dynamics Package and Assess Potential Halogen Bonds of Enoyl-ACP Reductase (FabI) Benzimidazole Inhibitors. *J. Comput. Chem.* **2016**, *37*, 836–847.

(108) Gaulton, A.; Bellis, L. J.; Bento, A. P.; Chambers, J.; Davies, M.; Hersey, A.; Light, Y.; McGlinchey, S.; Michalovich, D.; Al-Lazikani, B.; Overington, J. P. ChEMBL: A Large-Scale Bioactivity Database for Drug Discovery. *Nucleic Acids Res.* **2012**, *40*, D1100-7.

(109) Bento, A. P.; Gaulton, A.; Hersey, A.; Bellis, L. J.; Chambers, J.; Davies, M.; Krüger, F. A.; Light, Y.; Mak, L.; McGlinchey, S.; Nowotka, M.; Papadatos, G.; Santos, R.; Overington, J. P. The ChEMBL Bioactivity Database: An Update. *Nucleic Acids Res.* **2014**, *42*, D1083–D1090.

(110) Kim, Y.; de Castro, S.; Gao, Z.-G.; IJzerman, A. P.; Jacobson, K. A. Novel 2- and 4-Substituted 1 H -Imidazo[4,5- c]Quinolin-4-Amine Derivatives as Allosteric Modulators of the A 3 Adenosine Receptor. *J. Med. Chem.* **2009**, *52*, 2098–2108.

(111) Heitman, L. H.; Göblyös, A.; Zweemer, A. M.; Bakker, R.; Mulder-Krieger, T.; van Veldhoven, J. P. D.; de Vries, H.; Brussee, J.; IJzerman, A. P. A Series of 2,4-Disubstituted Quinolines as a New Class of Allosteric Enhancers of the Adenosine A 3 Receptor. *J. Med. Chem.* **2009**, *52*, 926–931.

(112) Slee, D. H.; Chen, Y.; Zhang, X.; Moorjani, M.; Lanier, M. C.; Lin, E.; Rueter, J. K.; Williams, J. P.; Lechner, S. M.; Markison, S.; Malany, S.; Santos, M.; Gross, R. S.; Jalali, K.; Sai, Y.; Zuo, Z.; Yang, C.; Castro-Palomino, J. C.; Crespo, M. I.; Prat, M.; Gual, S.; Díaz, J.-L.; Saunders, J. 2-Amino- N -Pyrimidin-4-Ylacetamides as A 2A Receptor Antagonists: 1. Structure–Activity Relationships and Optimization of Heterocyclic Substituents. *J. Med. Chem.* **2008**, *51*, 1719–1729.

(113) Francis, J. E.; Webb, R. L.; Ghai, G. R.; Hutchison, A. J.; Moskal, M. A.; DeJesus, R.; Yokoyama, R.; Rovinski, S. L.; Contardo, N. Highly Selective Adenosine A2 Receptor Agonists in a Series of N-Alkylated 2-Aminoadenosines. *J. Med. Chem.* **1991**, *34*, 2570–2579.

(114) Siddiqi, S. M.; Jacobson, K. A.; Esker, J. L.; Olah, M. E.; Ji, X.; Melman, N.; Tiwari, K. N.; Secrist, J. A.; Schneller, S. W. Search for New Purine- and Ribose-Modified Adenosine Analogs as Selective Agonists and Antagonists at Adenosine Receptors. *J. Med. Chem.* **1995**, *38*, 1174–1188.

(115) Roelen, H.; Veldman, N.; Spek, A. L.; von Frijtag Drabbe Künzel, J.; Mathôt, R. A. A.; IJzerman, A. P. N 6 ,C8-Disubstituted Adenosine Derivatives as Partial Agonists for Adenosine A 1 Receptors. *J. Med. Chem.* **1996**, *39*, 1463–1471.

(116) Tchilibon, S.; Joshi, B. V; Kim, S.-K.; Duong, H. T.; Gao, Z.-G.; Jacobson, K. A. No Title. *J. Med. Chem.* **2005**, *48*, 1745–1758.

(117) Cheong, S. L.; Venkatesan, G.; Paira, P.; Jothibasu, R.; Mandel, A. L.; Federico, S.; Spalluto, G.; Pastorin, G. Pyrazolo Derivatives as Potent Adenosine Receptor Antagonists: An Overview on the Structure-Activity Relationships. *Int. J. Med. Chem.* **2011**, *2011*, 1–15.

(118) Stoddart, L. A.; Vernall, A. J.; Denman, J. L.; Briddon, S. J.; Kellam, B.; Hill, S. J. Fragment Screening at Adenosine-A3 Receptors in Living Cells Using a Fluorescence-Based Binding Assay. *Chem. Biol.* **2012**, *19*, 1105–1115.

(119) Vauquelin, G. Effects of Target Binding Kinetics on in Vivo Drug Efficacy: Koff , Kon and Rebinding. *Br J Pharmacol.* **2016**, *173*, 2319–2934.

(120) Liu, K.; Kokubo, H. Exploring the Stability of Ligand Binding Modes to Proteins by Molecular Dynamics Simulations: A Cross-Docking Study. *J. Chem. Inf. Model.* **2017**, *57*, 2514–2522.

(121) Guterres, H.; Im, W. Improving Protein-Ligand Docking Results with High-Throughput Molecular Dynamics Simulations. *J. Chem. Inf. Model.* **2020**, *60*, 2189–2198.

(122) Glukhova, A.; Thal, D. M.; Nguyen, A. T.; Vecchio, E. A.; Jörg, M.; Scammells, P. J.; May, L. T.; Sexton, P. M.; Christopoulos, A. Structure of the Adenosine A1Receptor Reveals the Basis for Subtype Selectivity. *Cell* **2017**, *168*, 867–877.

(123) Matricon, P.; Ranganathan, A.; Warnick, E.; Gao, Z.-G.; Rudling, A.; Lambertucci, C.; Marucci, G.; Ezzati, A.; Jaiteh, M.; Dal Ben, D.; Jacobson, K. A.; Carlsson, J. Fragment Optimization for GPCRs by Molecular Dynamics Free Energy Calculations: Probing Druggable Subpockets of the A 2A Adenosine Receptor Binding Site. *Sci. Rep.* **2017**, *7*,

6398.

(124) Rodríguez, D.; Gao, Z.-G. G.; Moss, S. M.; Jacobson, K. A.; Carlsson, J.; Rodr??guez, D.; Gao, Z.-G. G.; Moss, S. M.; Jacobson, K. A.; Carlsson, J. Molecular Docking Screening Using Agonist-Bound GPCR Structures: Probing the A2A Adenosine Receptor. *J. Chem. Inf. Model.* **2015**, *55*, 550–563.

(125) Bolcato, G.; Bissaro, M.; Deganutti, G.; Sturlese, M.; Moro, S. New Insights into Key Determinants for Adenosine 1 Receptor Antagonists Selectivity Using Supervised Molecular Dynamics Simulations. *Biomolecules* **2020**, *10*, 732.

(126) Jespers, W.; Schiedel, A. C.; Heitman, L. H.; Cooke, R. M.; Kleene, L.; van Westen, G. J. P.; Gloriam, D. E.; Müller, C. E.; Sotelo, E.; Gutiérrez-de-Terán, H. Structural Mapping of Adenosine Receptor Mutations: Ligand Binding and Signaling Mechanisms. *Trends Pharmacol. Sci.* **2018**, *39*, 75–89.

(127) Lane, J. R.; Klein Herenbrink, C.; van Westen, G. J. P.; Spoorendonk, J. A.; Hoffmann, C.; IJzerman, A. P. A Novel Nonribose Agonist, LUF5834, Engages Residues That Are Distinct from Those of Adenosine-Like Ligands to Activate the Adenosine A 2a Receptor. *Mol. Pharmacol.* **2012**, *81*, 475–487.

(128) Gao, Z.-G. G.; Chen, A.; Barak, D.; Kim, S. K.; Müller, C. E.; Jacobson, K. A. Identification by Site-Directed Mutagenesis of Residues Involved in Ligand Recognition and Activation of the Human A 3 Adenosine Receptor. *J. Biol. Chem.* **2002**, *277*, 19056–19063.

(129) Kim, J.; Wess, J.; van Rhee, A. M. M.; Schöneberg, T.; Jacobson, K. A. K. A. Site-Directed Mutagenesis Identifies Residues Involved in Ligand Recognition in the Human A Adenosine Receptor. *J. Biol. Chem.* **1995**, *270*, 13987–13997.

(130) Kim, J.; Jiang, Q.; Glashofer, M.; Yehle, S.; Wess, J.; Jacobson, K. A. Glutamate Residues in the Second Extracellular Loop of the Human A2a Adenosine Receptor Are Required for Ligand Recognition. *Mol. Pharmacol.* **1996**, *49*, 683–691.

(131) Guo, D.; Pan, A. C.; Dror, R. O.; Mocking, T.; Liu, R.; Heitman, L. H.; Shaw, D. E.; IJzerman, A. P. Molecular Basis of Ligand Dissociation from the Adenosine A 2A Receptor. *Mol. Pharmacol.* **2016**, *89*, 485–491.

(132) Barkan, K.; Lagarias, P.; Stamatis, D.; Vrontaki, E.; Klotz, K.-L.; Kolocouris, A.; Ladds, G. Pharmacological Characterisation of Novel Adenosine Receptor A3AR Antagonists. *Sci. Rep.* **2020**, *10*, 20781.

(133) Bertheleme, N.; Singh, S.; Dowell, S. J.; Hubbard, J.; Byrne, B. Loss of Constitutive Activity Is Correlated with Increased Thermostability of the Human Adenosine A 2A Receptor. *Br. J. Pharmacol.* **2013**, *169*, 988–998.

(134) Jiang, Q.; Lee, B. X.; Glashofer, M.; Van Rhee, A. M.; Jacobson, K. A. Mutagenesis Reveals Structure-Activity Parallels between Human A(2A) Adenosine Receptors and Biogenic Amine G Protein-Coupled Receptors. *J. Med. Chem.* **1997**, *40*, 2588–2595.

(135) Jiang, Q.; Van Rhee, A. M.; Kim, J.; Yehle, S.; Wess, J.; Jacobson, K. A. Hydrophilic Side Chains in the Third and Seventh Transmembrane Helical Domains of Human A2A Adenosine Receptors Are Required for Ligand Recognition. *Mol. Pharmacol.* **1996**, *50*, 512–521.

(136) Pohorille, A.; Jarzynski, C.; Chipot, C. Good Practices in Free-Energy Calculations. *J. Phys. Chem. B* **2010**, *114*, 10235–10253.

(137) Deflorian, F.; Perez-Benito, L.; Lenselink, E. B.; Congreve, M.; van Vlijmen, H. W. T.; Mason, J. S.; Graaf, C. de; Tresadern, G. Accurate Prediction of GPCR Ligand Binding Affinity with Free Energy Perturbation. *J. Chem. Inf. Model.* **2020**, *60*, 5563–5579.

(138) Wan, S.; Potterton, A.; Husseini, F. S.; Wright, D. W.; Heifetz, A.; Malawski, M.; Townsend-Nicholson, A.; Coveney, P. V. 20190128. *Interface Focus* **2020**, *10*, 20190128.

(139) Keränen, H.; Åqvist, J.; Gutiérrez-de-Terán, H. Free Energy Calculations of A2A Adenosine Receptor Mutation Effects on Agonist Binding. *Chem. Commun.* **2015**, *51*, 3522–3525.

(140) Cappel, D.; Hall, M. L.; Lenselink, E. B.; Beuming, T.; Qi, J.; Bradner, J.; Sherman, W. Relative Binding Free Energy Calculations Applied to Protein Homology Models. *J. Chem. Inf. Model.* **2016**, *56*, 2388–2400.

(141) Hoare, S. R. J.; Fleck, B. A.; Williams, J. P.; Grigoriadis, D. E. The Importance of Target Binding Kinetics for Measuring Target Binding Affinity in Drug Discovery: A Case Study from a CRF1 Receptor Antagonist Program. *Drug Discov. Today* **2020**, *25*, 7–14.

(142) Dawson, E. S.; Wells, J. N. Determination of Amino Acid Residues That Are Accessible from the Ligand Binding Crevice in the Seventh Transmembrane-Spanning Region of the Human A1 Adenosine Receptor. *Mol. Pharmacol.* **2001**, *59*, 1187–1195.

TOC GRAPHIC

$\Delta\Delta G_{bind,EXP} = -2.24 \pm 0.20$

$\Delta\Delta G_{bind',TI/MD} = -3.05 \pm 0.05$

A17

A_1R K_d = 5.62 nM

    RT = 41.33 min

A_3R K_d = 13.5 nM

    RT = 47.23 min